Love wave tomography of the central Tien Shan from ambient seismic noise

---

A Thesis

Presented to

the Faculty of the Department of Earth and Atmospheric Sciences

University of Houston

In Partial Fulfillment

of the Requirements for the Degree

Master of Science

By

Xu Wang

May 2013

Love wave tomography of the central Tien Shan from ambient seismic noise

Xu Wang

APPROVED:

_____

Dr. Aibing Li

_____

Dr. Alexander Robinson

_____

Dr. Ching-Wen Chen

_____

Dean, College of Natural Sciences and Mathematics

I express gratitude to Dr. Aibing Li, Dr. Alexander Robinson, and Dr. Ching-Wen Chen for their suggestions and direction in writing and revising this thesis. Also I am thankful for the understanding and support of my parents who never give up on me. I am most grateful for Qun He, my sweet and very patient wife, for her continuous love on me.

Love wave tomography of the central Tien Shan from ambient seismic noise

---

An Abstract of a Thesis

Presented to

the Faculty of the Department of Earth and Atmospheric Sciences

University of Houston

In Partial Fulfillment

Of the Requirements for the Degree

Master of Science

By

Xu Wang

May 2013

Abstract

The Tien Shan is the world's largest and most active intracontinental orogeny. Despite numerous geological and geophysical studies conducted in the Tien Shan, the mountain-building mechanisms remain debatable. There are three competing hypotheses: (1) underthrusting of the Kazakh and Tarim lithosphere on both sides of the Tien Shan, (2) coherent shortening in the Tien Shan lithosphere, and (3) up-welling of hot mantle beneath the central Tien Shan. To better understand the formation of the Tien Shan crust and distinguish the competing models, I applied the ambient noise tomography method to Love waves in the central Tien Shan at 40 seismic stations and obtained phase velocities at a period range of 8 s-35 s. The noise data were first processed at individual stations with instrument response removal, component rotation and spectral whitening. Then cross-correlations of ambient noise were computed on a daily basis and then stacked for each station pair. Love wave phase velocities were computed from the stacked waveforms.

Four Love wave phase velocity anomaly zones are imaged in the central Tien Shan. A high velocity anomaly is consistently present in the Kazakh Shield. Another high velocity zone is observed at the boundary between the Tarim basin and the Tien Shan from 18 to 35 s. This anomaly becomes stronger and extends more towards the Tien Shan at longer periods. Such high velocity anomalies most likely reflect strong crust beneath the Kazakh shield and the Tarim basin. The northward extension of the second fast anomaly suggests that the Tarim lithosphere probably

underthrusts beneath the Tien Shan. Two significant low velocity zones are imaged in the southwest and central-east of the study area, which correlate with high deformation mountain ranges. These low phase velocities might be due to high temperature or high volatile content in the Tien Shan crust, suggesting a weak crust beneath the Tien Shan. The slow anomaly at relatively long periods could also reflect a thick crust root beneath the mountain ranges. These results suggest that the Tien Shan was formed by coherent shortening of its weak lithosphere which is sandwiched between the two relatively strong lithospheres of the Kazakh shield and the Tarim basin.

Content

1. Introduction

The Tien Shan mountain belt is unique due to its intracontinental location and complex orogens. It is located in central Asia, more than 2000 km of the India-Asia suture. The Tien Shan consists of a series of east-west trending ranges that resulted as a collage of many continental blocks, islands arcs and accretionary prisms after the closure of roughly east-west trending ocean basins at the end of Paleozoic and early Mesozoic (Burtman, 2010; Xiao et al., 2012). The large scale NEE-SWW trending thrust faults and earthquakes dominate the present surface deformation as a result of the ongoing a north to south compression (Abdrakhmatov et al., 1996; Xu et al., 2008; Yang et al., 2008).

Numerous geophysical studies (Vinnik et al., 2004 and 2007; Jiang et al., 2010; Guoet al., 2010; Li et al., 2010b; Lei, 2011; Lisi et al., 2012) have been conducted in the Tien Shan area to understand its crustal and mantle structure. Three hypotheses have been proposed to explain the Cenozoic formation and evolution of the Tien Shan. Fleitout and Froidevaux (1982) suggested that the mountain building is due to shortening in the crust accompanied by similar movement in the mantle lithosphere, while Roecker et al. (1993) claimed that the Tien Shan orogenic belt was caused by the underthrusting of the Tarim and Kazakh lithosphere based on body wave seismic tomography. In addition, Omuralieva et al. (2009) proposed that the

upwelling of hot mantle beneath the Tien Shan was responsible for building the mountain belt.

It is clear that there is no general agreement among previous studies about the mechanism of the Tien Shan formation. To find further evidence to support or disprove the existing mechanisms, I obtained Love wave phase velocity from ambient noise tomography in the central Tien Shan area. The phase velocity maps from 8 to 35s shed new light on the Tien Shan crustal formation.

1.1 Geological setting and history

The Tien Shan, the most prominent mountain belt of central Asia, is located ~2000 km north of the India-Asia suture and extends ~2500 km in a WSW-ENE direction with a width of few hundred km (Lisi and Li, 2012). It is one of the youngest and most tectonically active intracontinental orogenies on Earth. The mountain belt is interpreted to be the result of the collision of the Indian subcontinent with the southern margin of Eurasia over the last 50 million years (Molnar and Tapponnier, 1975). The active intraplate mountain range sits within continental crust originated from the accretion of numerous Paleozoic terranes in Central Asia (Burtman, 1975) (**Figure 1**).

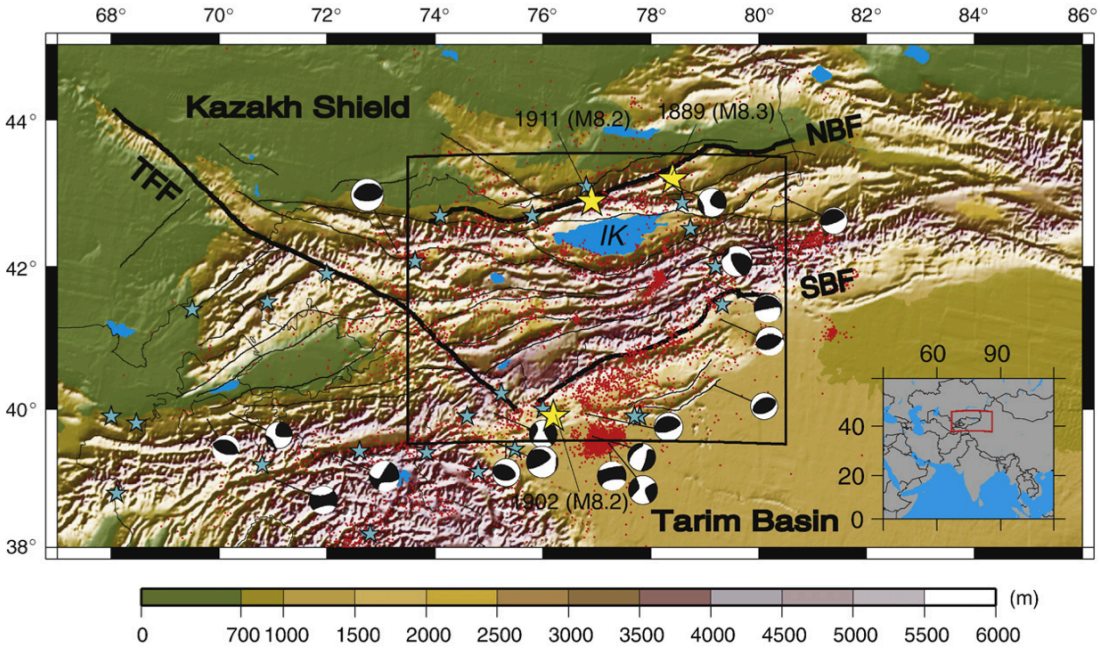

Figure 1. *Topographic Map of the Tien Shan Area (Omuralieva et al., 2009). The insert bottom right is the location of the Tien Shan. Black lines are regional and faults. Yellow and green stars depict historic earthquakes with M>=8.0 and 6.0<M<8.0. Red dots are earthquakes from 1998-2000. Focal mechanisms are from the Harvard CMT catalogue. The black-white balls are the focal mechanisms.*

The Tien Shan is bounded between the Kazakh shield in the north and Tarim basin in the south, both of which have been stable since Precambrian. The Tien Shan can be divided into three main blocks; the northern Tien Shan, middle Tien Shan, and southern Tien Shan (Aiymjan, 2009). These terrane divisions are separated by the Nikolaev Line- North Nalati Fault and Atbashi-Ingylchek-South Nalati-Qawabulak Fault. Intracontinental deformation, mostly strike-slip and normal faulting, characterized the Permian and Triassic periods over much of the Tien Shan and Dzhungar Basin (**Figure 2**).

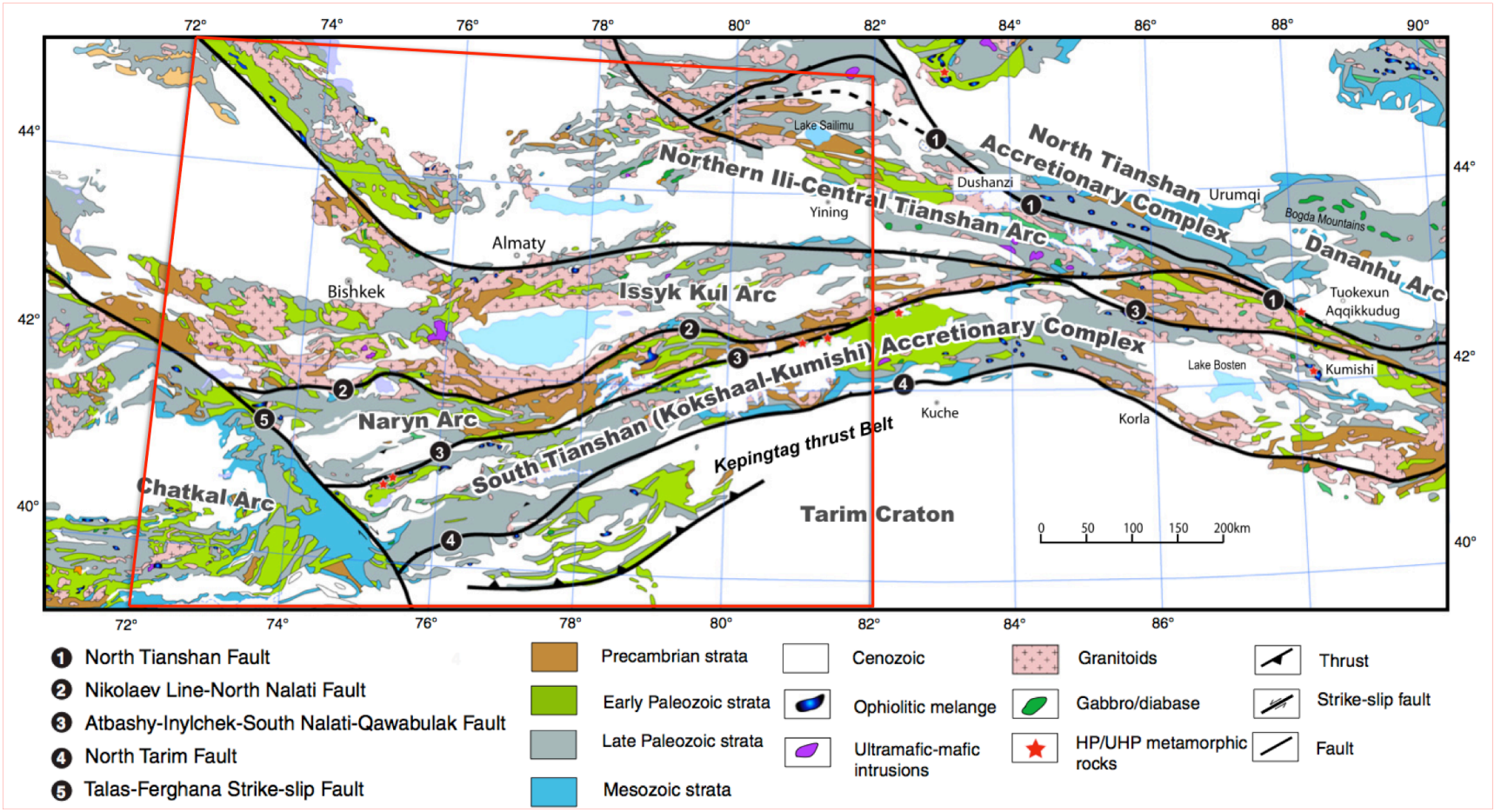

Figure 2. *Geological and tectonic map of the Tien Shan orogenic collage showing major Paleozoic magmatic arcs and the Faults (Xiao et al., 2012). Red frame is the work area of this study.*

Xiao et al. (2012) proposed a tectonic model of two Paleozoic collisional events during the accretion of the Tien Shan mountain ranges. The first event was during the Ordovician- early Silurian when the island arcs near the Kazakhstan Craton (North Ili, Issyk Kul, and Chatkal) developed in the northern part of the Paleo- Asian Ocean, and continuously accreted to the north and form the northern Tien Shan block (Xiao et al., 2012; Bullen et al., 2003). The second event occurred along the southern boundary of the South Tien Shan and Tarim Basin in the early Carboniferous, which involved the collision with the Tarim Craton. The roughly NS compression was resumed about 20-25 Ma (Sobel and Dumitru, 1997; Yang and Liu, 2002) is still undergoing. GPS velocity measurements indicated that the shortening in the north to south direction at a rate of ~20mm per year (Abdrakhmatov et al., 1996).

1.2 Previous works

Although several geophysical studies (e.g. Vinnik, 2004, 2006; Lei 2010 et al.) have been done within the Tien Shan area, the mechanism of Tien Shan formation still remains debatable. Previous studies (e.g. Guo, 2010; Lisi and Li, 2012) usually provided seismic information from upper crust to upper mantle. However, even at the same depth interval, each methodology has conveyed a different result and therefore different interpretations.

1.2.1 Upper and middle crust

Vinnik et al. (2004) conducted receiver function study in the central Tien Shan and showed that the velocities beneath the middle Tien Shan are generally low in the mid crust (**Figure 3 a**), indicating a weak crust. Similar result was also found by Lisi and Li (2012) in their study of Rayleigh wave phase velocity

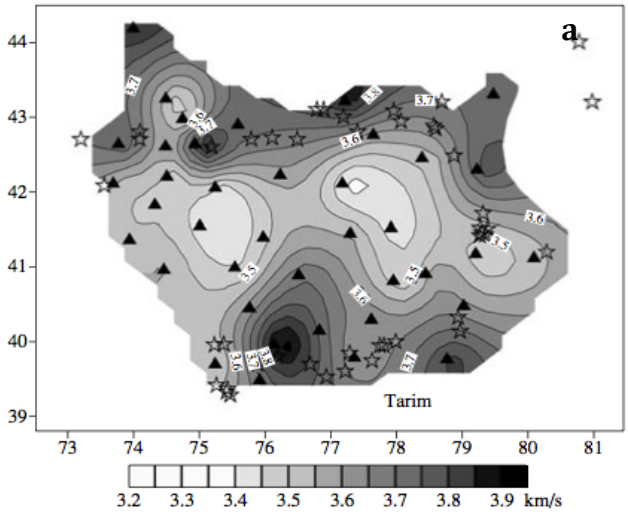

Figure 3. *a : Averaged S velocity within the crust in the depth interval from 10 km to 35 km. b : Averaged S velocity for the mantle in the depth interval from 70 to 90 km. c: Averaged S velocity for the mantle in the depth interval from 110 to 130 km. d : Thickness of the crust. The figure is from Vinnik et al., (2006).*

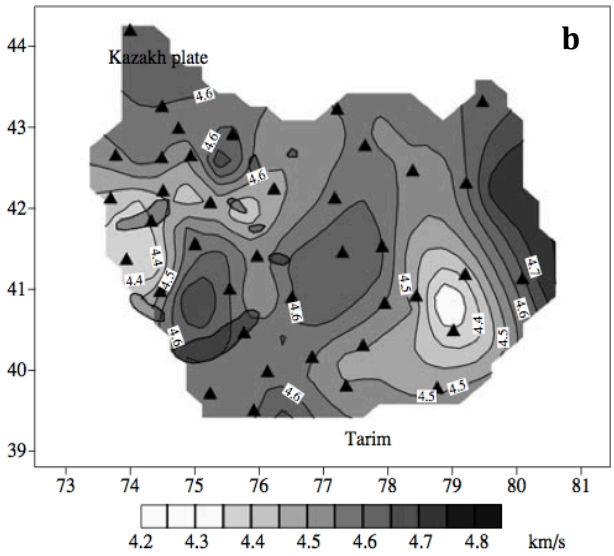

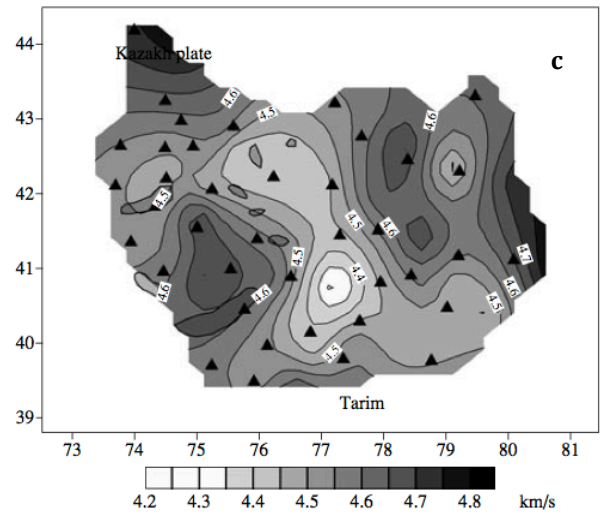

Figure 3. *(Continued)*

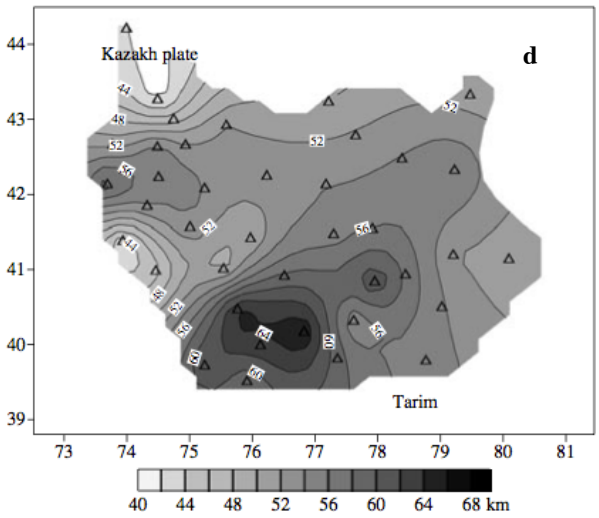

Figure 3. *(Continued)*

Lisi and Li (2012) imaged a low velocity zone in Tien Shan area and a fast velocity zone near the boundaries of Tien Shan-Kazakh Shield and Tien Shan-Tarim basin at the short periods (20s-50s) (**Figure 4**). They interpreted the low velocity zone around the central Tien Shan as evidence for a thick crust. Crustal thickness map (Vinnik et al., 2006) shows that the Kazakh shield and the Tien Shan foreland are characterized by a 50 km thick crust. The thickest crust of 70 km is located in southwest of the central Tien Shan, and the thinnest crust of 40 km is located around the Talas-Fergana fault (**Figure 3 d**). Shear wave splitting study (Li et al. 2010b) describes the most fast polarization direction for the upper layers is consistent with the mountain strikes, which is normal to the regional maximum compression stress (**Figure 5**). Researchers (e.g. Makeyeva et al., 1992; Li and Chen, 2006) suggested that the dominant fast direction at most stations, along to the

mountain belt, is due to the collision force transported from plate boundary between the India and Eurasia.

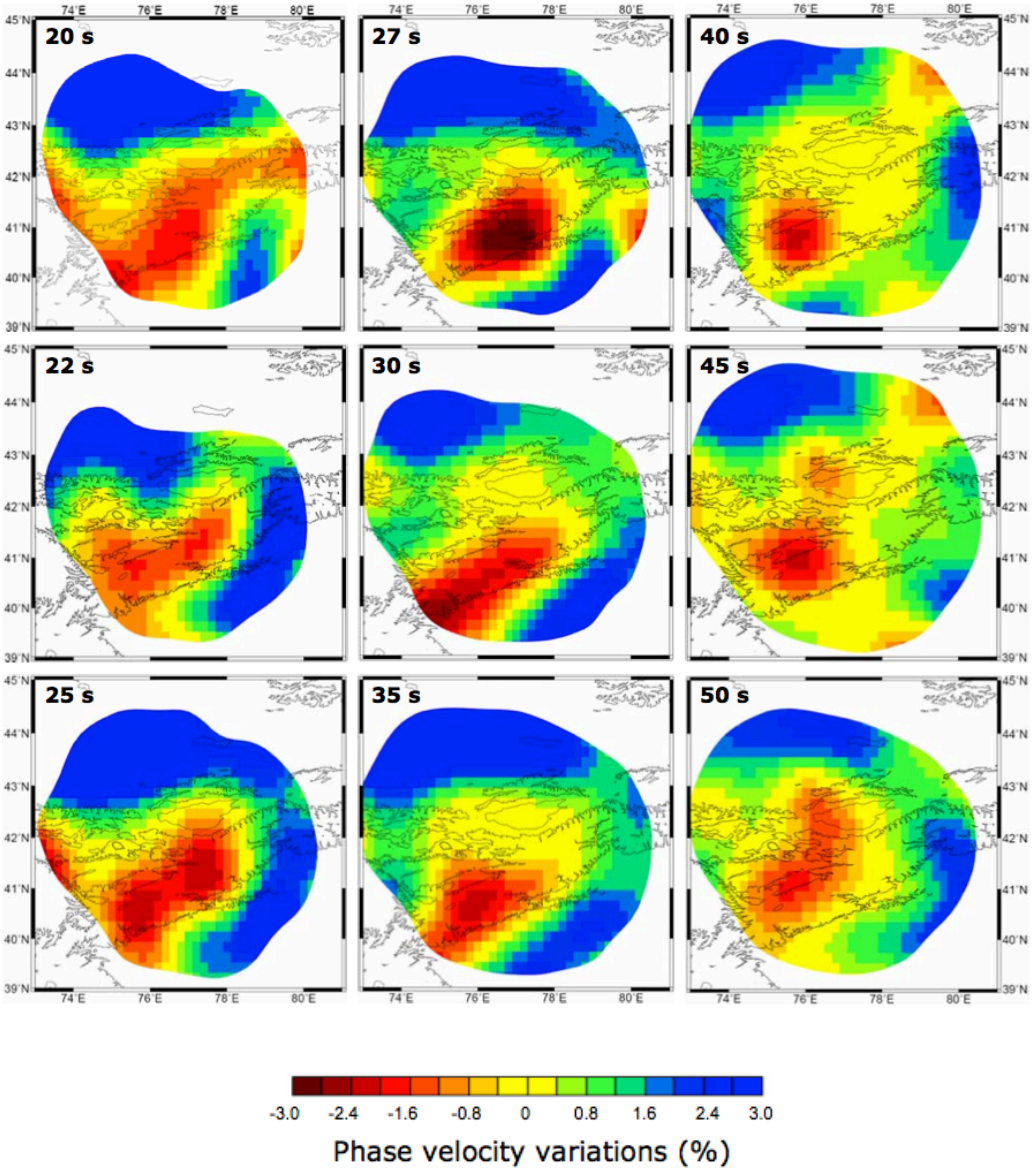

Figure 4. *Phase velocity variation maps of Rayleigh wave in the Tien Shan at periods from 20s to 50s.*

The studies of Lisi and Li (2012) and Vinnik et al. (2004, 2006) found two high velocity zones along the boundaries between the Tien Shan and the Kazakh Shield to

the north and the Tien Shan to the Tarim Basin to the north. The high velocity zone suggested that the Tien Shan is sandwiched by two rigid parts (**Figure 3 a** and **Figure 4**).

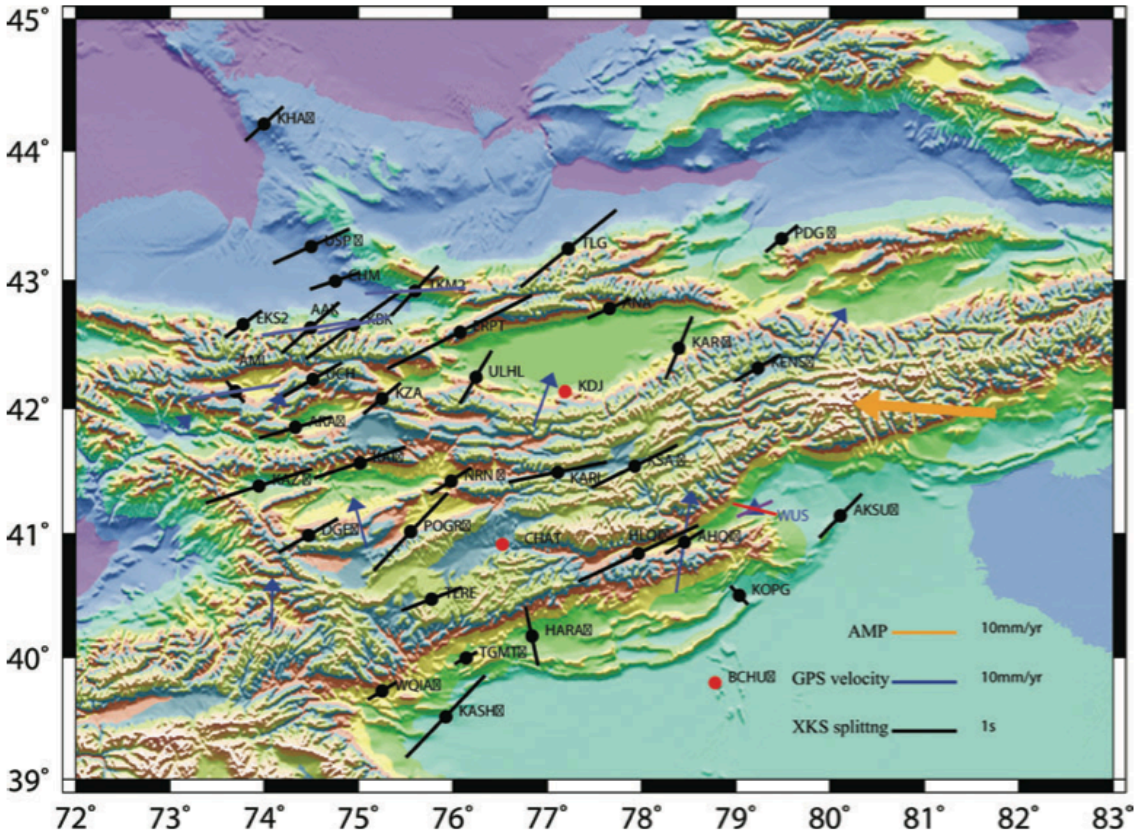

Figure 5. *Distribution of stations of the Tien Shan. The circles are nulls. Black and steel gray line segments are statistically distinct-splitting parameters. (Li et al., 2010)*

Different velocity maps for the central Tien Shan have been developed by other scientists (Guo et al., 2010 and Lei, 2011). Guo et al. (2010) performed Ambient Noise Tomography of Rayleigh waves in the Tien Shan area and their main results are shown in **Figure 6**. At short periods of 9 and 20s (~10-25 km in depth), phase velocity maps (**Figure 6 a,b**) show that the central Tien Shan is dominated by low

velocity anomalies. The low velocity region becomes smaller at the period of 30s (**Figure 6 c**). Guo et al. (2010) interpreted that the low velocity zone near the west Tien Shan is a consequence of extensive fractured and fluid-filled rocks. As the depth increases, the low velocity zone shrinks into a narrow zone. The high velocity zones, which lie along the north and south boundaries of the Tien Shan, are the indicators of underthrusting of the Kazakh Shield and Tarim Basin.

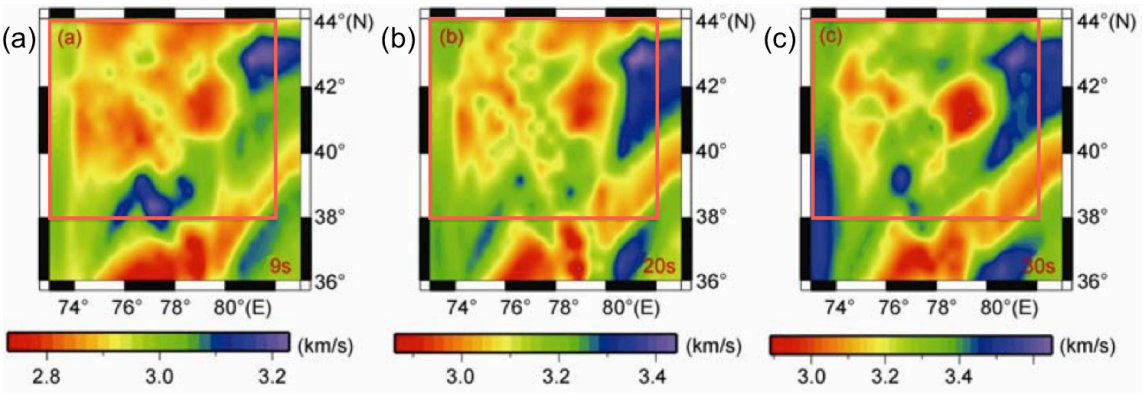

Figure 6. *Rayleigh wave phase velocity distributions at 9s (a), 20s (b) and 30s (c). (Guo et al., 2010)*

Lei (2010) measured the P- and S-wave velocity with in the Tien Shan, which showed a high velocity anomaly in the crust of Tien Shan, contrary to what was found by Vinnik et al. (2004). Lei's study showed a low P and S wave velocity with a low Poisson's Ratio anomaly zone that is beneath a zone of high P and S wave velocity and low Poisson's Ratio. Near the boundaries of Tien Shan to Tarim Basin (south) and Kazakh Shield (north), the velocities of P and S waves are high and the Poisson's ration is low, which means strong lithosphere exists beneath Tarim and Kazakh areas (**Figure 7**). Those high velocity zones move toward each other with

the depth, Lei interpreted this as underthrusting of the Kazakh and Tarim blocks that helped to raise the Tien Shan Mountain.

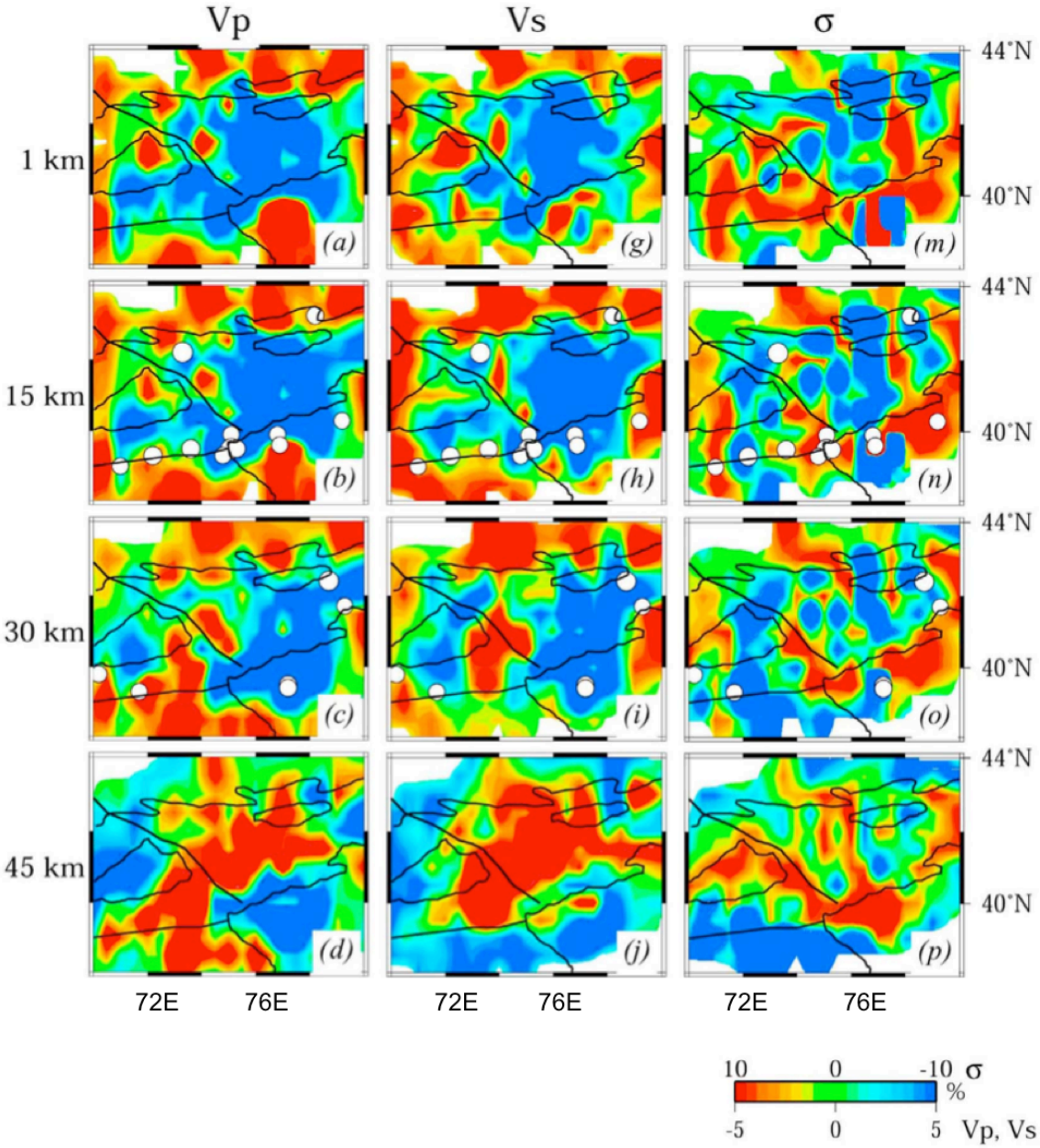

Figure 7. *Results of Vp, Vs, and Poisson's Ratio* σ *tomography images in map view. Red color denotes low velocities and high Poisson's Ratio; blue color denotes the high velocities and low Poisson's Ratio (depth from 1-45km) (Lei, 2010).*

1.2.2 Lower crust and upper mantle

In the study of Vinnik et al. (2006), two low velocity zones exist within the central Tien Shan area, a southeast low velocity zone and a northwest low velocity zone. They suggested the two low velocity zones corresponded to small-volume outflows of basalts (**Figure 3 b**). At depth of upper mantle (**Figure 3 c**), the low velocity anomaly is along the mountain range direction. This may be caused by the extension of mantle along the mountain strike, and the compressed mantle in the direction normal to the mountain belt. Based on the observation of a low velocity and high Poisson ratio (Lei, 2010) combined with a thinner crust thickness (Vinnik ,2006 and Tian, 2010), Lei (2010) believed mantle upwelling from occurs beneath the central Tien Shan, (**Figure 8 and Figure 3 c**).

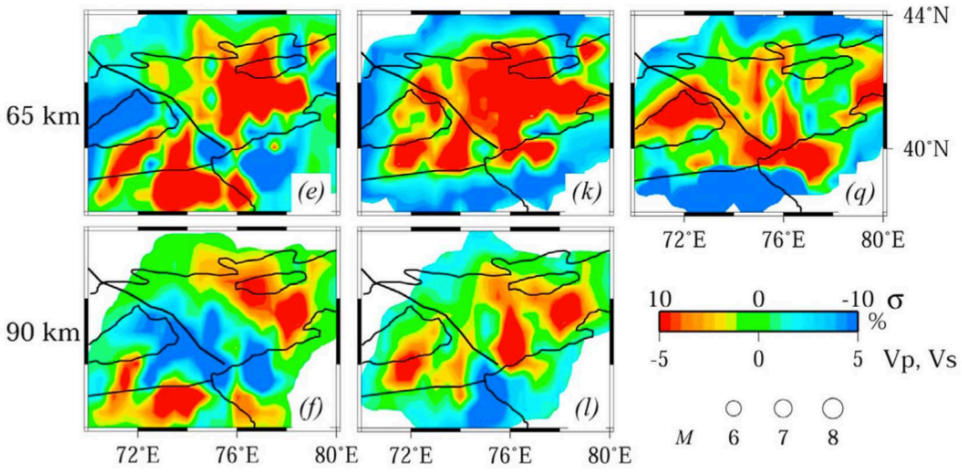

Figure 8. *Results of Vp, Vs, and Poisson's Ratio* σ *tomography images in map view. Red color denotes low velocities and high Poisson's Ratio; blue color denotes the high velocities and low Poisson's Ratio (Depth from 65-90km) (Lei, 2010).*

1.2.3 Hypothesizes

Based on the shear wave splitting study and GPS velocity study, scientists (e.g. England and Houseman, 1985) believe that the uplift of Tien Shan is caused by internal shortening of the compression from the Kazakh Shield and Tarim Basin. Under this suggestion, the central Tien Shan is sandwiched between the two rigid blocks, and the crust beneath Tien Shan is comparatively weaker than the crust under the Tarim and the Kazakh Shield. According to the velocity anomaly map (e.g. Vinnik et al., 2007), the velocity around the central Tien Shan should be low and the stronger blocks (Kazakh Shield and Tarim Basin) on both sides should have higher velocity comparing with the central parts (**Figure 9-a**).

In the second model, the formation of the Tien Shan is due to underthrusting of the Kazakh and Tarim lithosphere on both sides of Tien Shan (Lei and Zhao, 2007; Li et al., 2009). According to this characterization, there should be a "transition zone" between the stronger blocks (Kazakh Shield or Tarim Basin) and the central Tien Shan. The velocity around the transition zone is lower than the strong block's at the shallow layers and should increase with the depth (longer period in the ambient noise velocity maps). As for the central Tien Shan mountain part, the velocity may be higher than the transition zone due to less deformation in the central part.

Another assumption for the formation of the Tien Shan is related more to the mantle activation beneath the Tien Shan. Some papers have identified a significant low

velocity zone under the Tien Shan (Omuralieva et al., 2009)(**Figure 9-c**), which is usually overlain by a high velocity zone in the shallow layers. Some researchers (e.g. Xu et al., 2002; Pei et al., 2007) proposed that the deep low velocity zone beneath the central Tien Shan is related to melt supplied from the upper mantle. As for the strong block of Tarim Basin and Kazakh Shield, the velocity is higher than the central Tien Shan.

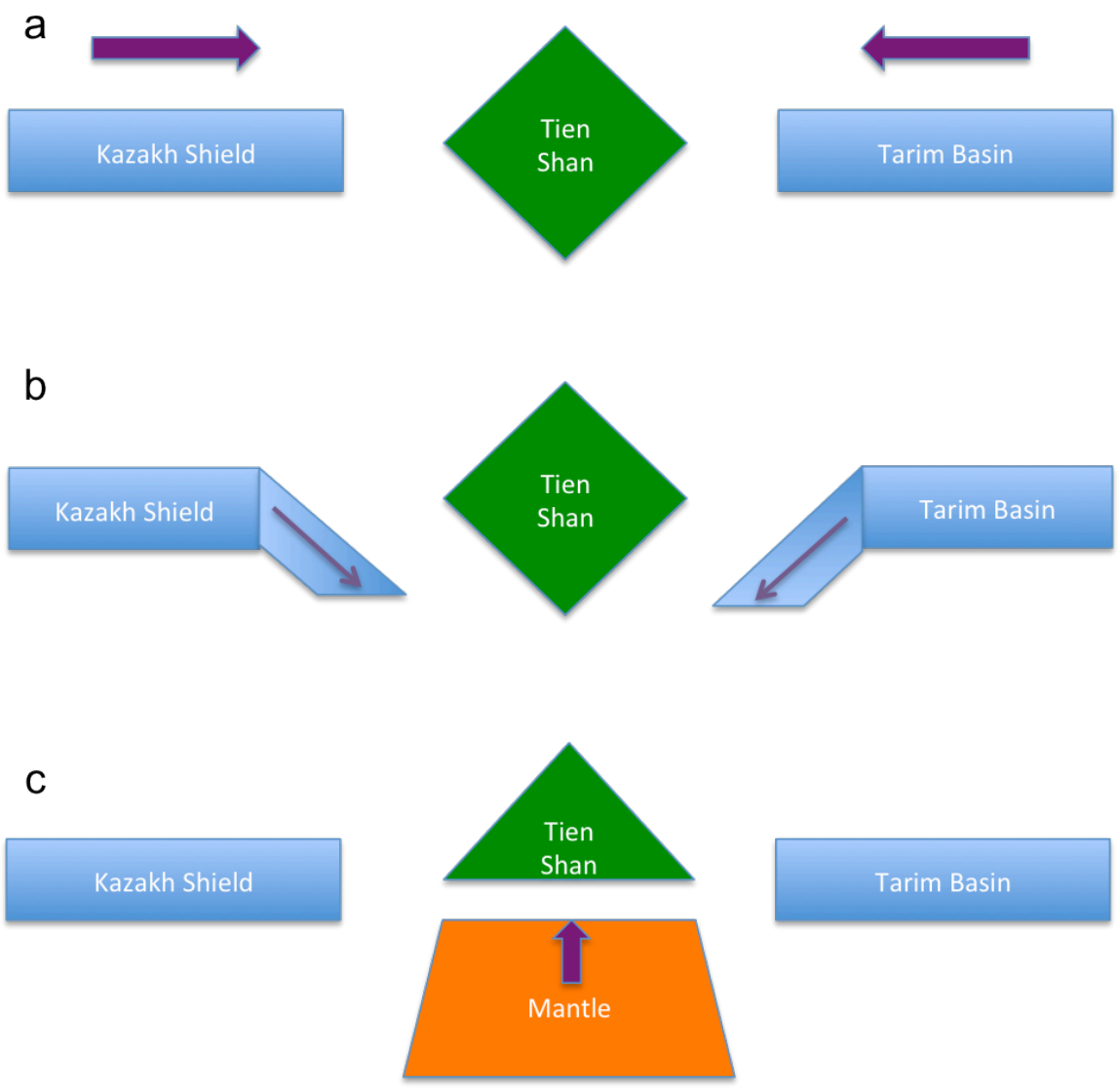

Figure 9. *Cartons of existing models for the formation of the Tien Shan. Green is mountain formation, blue is crust, red represents for the melt supplied from mantle and yellow is mantle. (a) Model of the suggestion of tectonic collision mountain formation. (b) The model of the suggestion of plates under thrusting mountain formation. (c) The model of mantle upwelling mountain formation.*

1.3 Motivation

As shown above, the Tien Shan has been well studied using different geophysical data and methods. However, different studies suggested different mechanisms for the Tien Shan formation. Despite Rayleigh wave tomography has been applied in a big area including the Tien Shan from ambient noise data (Guo et al., 2010), the model has poor resolution in the Tien Shan. To complement existing studies in the Tien Shan and better image the crustal structure, I applied seismic ambient noise tomography to Love waves in the central Tien Shan area. Love wave is sensitive to SH wave velocity while Rayleigh wave is mainly affected by SV wave velocity. Love wave phase velocity in the Tien Shan therefore could provide new information for the crustal structure and help to understand the formation of the Tien Shan.

The goal of this study is to develop Love wave phase velocity maps in the Tien Shan from ambient noise tomography. Below I introduce the method in section 2, and describe data origin and data processing procedures in section 3, show phase velocity measurements at station pairs and phase velocity maps in section 4, discuss the interesting observed features in section 5, and give the conclusion in section 6.

2. Methodology of Ambient Noise Tomography

Ambient Noise Tomography is a method of using interferometry to image subsurface seismic velocity variations using seismic surface waves extracted from the background ambient vibrations of the Earth (Heather, 2012). The Green function between two stations can be estimated from the cross correlation of diffuse wave fields (Weaver and Lobkis, 2001). The first application of ambient noise study for surface wave tomography was carried out in 2005 in southern California (Shapiro et al., 2005). This study used ambient noise tomography to measure the group velocity over a very short range of periods (7.5-15). The group velocity maps displayed velocity variations related to geological formations, with low velocities correlated to sedimentary basins and high velocity zones correlated to mountain ranges. The method of ambient noise tomography has been increasingly applied in the study of tectonically active areas (Bensen et al., 2007; Lin et al., 2008; Guo, 2010; Li et al., 2010a).

The theory of Ambient Noise Tomography is supported by the following experiment. Assuming that two receivers are surrounded by thousands of seismic events (sources) (**Figure 10**) and the distribution of these sources is azimuthally homogeneous, these two stations will record the wave energy from all the surrounding events. The signals recorded at the two receivers are then cross-correlated. If the cross-correlations from all the sources are subsequently stacked, the energy that travelled along paths between these two receivers will add

constructively, whereas energy that did not travel along these paths will add destructively. The waveform after cross-correlation is very similar to surface waves. Hence the resulting signal will approximate the surface wave Green's Function between these the two receivers. Details for Rayleigh wave ambient noise tomography method are described by Bensen et al. (2007).

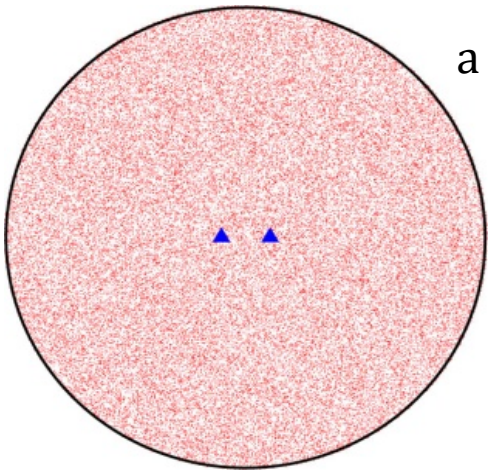

Figure10. *Theory of Cross-Correlation, a: two stations located in the random noise; b: the noise recorded by the traces of the stations in figure a; c: comparison of the result of two stations' cross-correlation (blue) with surface wave waveform (red).*

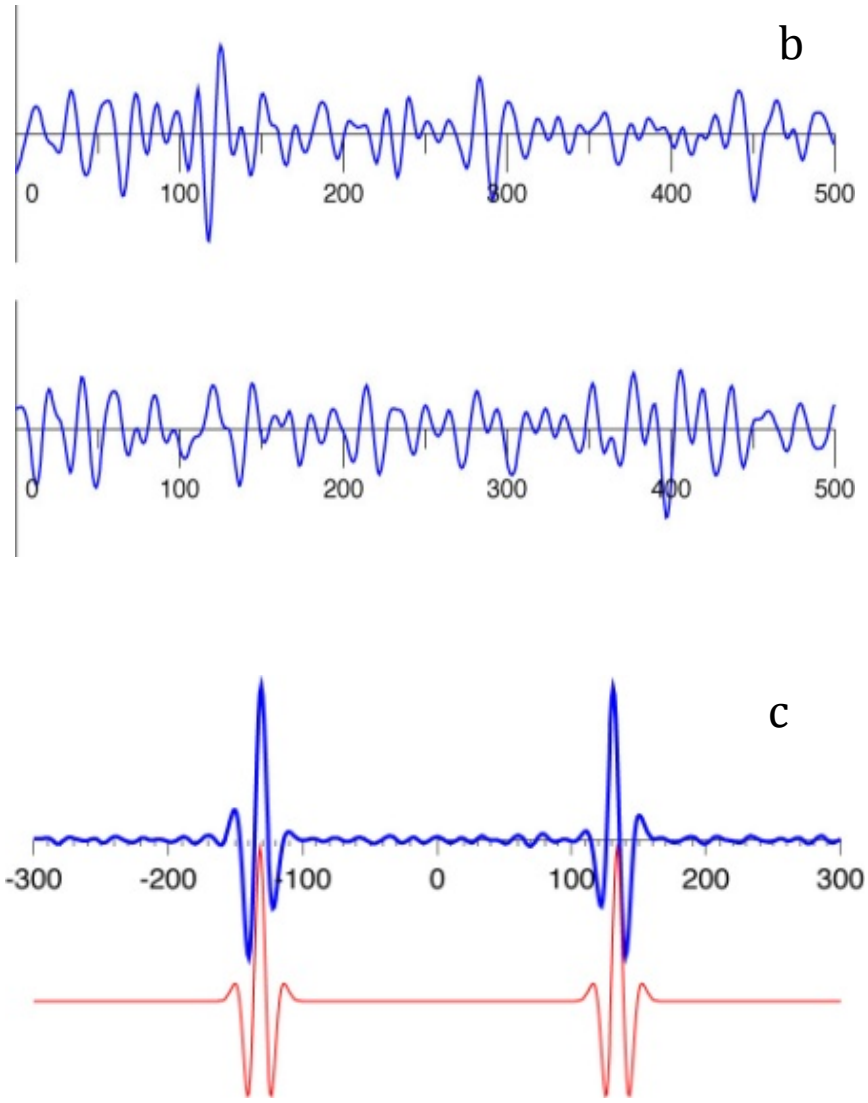

Figure10. *Theory of Cross-Correlation, a: two stations located in the random noise; b: the noise recorded by the traces of the stations in figure a; c: comparison of the result of two stations' cross-correlation (blue) with surface wave waveform (red). (Continued) (Li, Lecture in Seismic Analysis Code Course, 2012)*

The ambient seismic noise method has several advantages over traditional surface wave measurements from earthquake data (Bensen, 2007). First, since the ambient noise is random around the station, the recorded data will contain different directions. This avoids unsampled propagation directions that are ignored by direct surface wave measurement from the two-station method. Second, traditional inversions always depend on the priori information of the source, which is not always known. However, since the ambient noise tomography measures the 'noise', the location and other information of source are not needed. Third, the resolution from seismic ambient noise tomography can be improved by simply adding more stations within the study area. However, for traditional seismic studies, the resolution can hardly be controlled. The fourth advantage is that the ambient noise tomography preforms very well in surface wave dispersion especially at short periods less than 40 s since its signal to noise ratio can be improved by increasing the time records of ambient noise data. Teleseismic methods are difficult for surface wave dispersions at short periods due to the intrinsic attenuation and scattering from distant sources.

The ambient noise method also has its shortages. First, the noise is not as strong as the earthquake events, so the amplitude that we record may be very low, sometimes the "event" can only be identified after stacking. Another limitation of this method is that ambient noise tomography needs to be applied in networks that have a long operation time (e.g. one or two years), so that it can give a high signal-noise ratio result.

3. Data Origin and Processing

3.1 Data origin

The ambient noise data were requested from the IRIS (Incorporated Research Institutions for Seismology) for 40 stations in the central Tine Shan. Most stations were from the network of the Tien Shan Continental Dynamics and Kyrgyz Seismic Telemetry Network, data at the station of WUS is a part of the Geoscope. The station of TLG is contributed from the network of Kazakhstan Network. All stations are equipped with three component broadband sensors (**Figure 11)**. The operation time period was from September 1999 to July 2000. The station location and sensor information are listed in **Table 1.** The data from IRIS is in seed format, which were transferred to SAC format using RdSeed software. The following data processing was conducted using Seismic Analyzing Code (SAC) under Linux environment. Seismograms are recorded along three components, which are north, east, and vertical. Since Love wave is only recorded on the two horizontal components, I processed the data only from the north and east components.

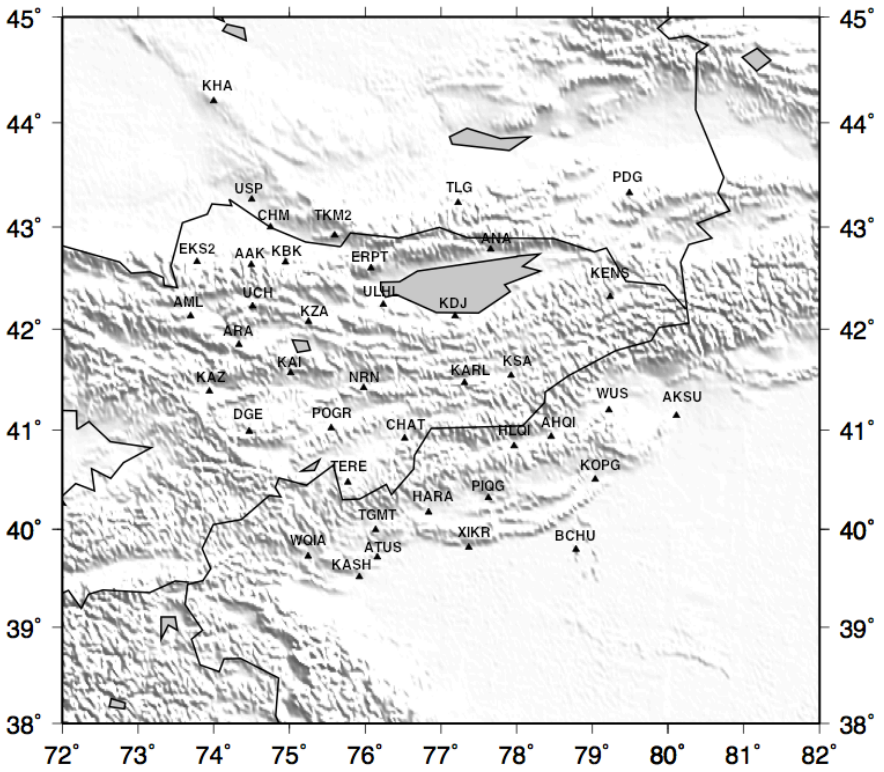

Figure 11. *Locations of stations*

Table 1, Stations Information

STATION	LONNGTIUDE	LATITUDE	POLES	ZEROS
AHQI	78.4578	40.9347	2	3
AKSU	80.1098	41.1441	5	3
ANA	77.657	42.7844	2	3
ARA	74.3292	41.8491	5	3
ATUS	76.1572	39.716	2	3
BCHU	78.7825	39.7933	2	3
CHAT	76.5209	40.918	5	3
DGE	74.469	40.9869	2	3
HARA	76.8367	40.1742	2	3
HLQI	77.9643	40.8415	2	3
KAI	75.0134	41.5681	2	3
KARL	77.3093	41.4733	2	3
KASH	75.9243	39.5165	2	3
KAZ	73.9437	41.3849	2	3
KDJ	77.1856	42.1326	2	3
KENS	79.2362	42.3201	5	3
KHA	73.9973	44.2081	2	3
KOPG	79.036	40.504	5	3
KSA	77.9257	41.5425	2	3
NRN	75.9792	41.423	2	3
PDG	79.4876	43.3275	2	3
PIQG	77.627	40.3204	5	3
POGR	75.5502	41.0183	2	3
TERE	75.7718	40.4757	5	3
TGMT	76.139	39.9956	5	3
WQIA	75.2473	39.7267	2	3
XIKR	77.3666	39.8178	5	3
AAK	74.4944	42.6333	5	3
AML	73.6941	42.1311	5	3
CHM	74.7513	42.9986	5	3
EKS2	73.7772	42.6615	5	3
ERPT	76.0735	42.6011	5	3
KBK	74.9478	42.6564	5	3
TKM2	75.5966	42.9208	5	3
UCH	74.5134	42.2275	5	3
USP	74.4997	43.2669	5	3
WUS	79.218	41.199	10	3
TLG	77.225	43.233	5	3

Table 1, Stations Information (Continued)

STATION	LONGITUDE	LATITUDE	POLES	ZEROS
KZA	75.2496	42.0778	5	3
ULHL	76.2417	42.2456	8	3

3.2 Data processing

Following the steps given by Bensen (2007) and Lin (2008), I designed my research workflow into three phases.

3.2.1 Single station preparation

The main purpose of the single station processing is to remove the instrumental irregularities that tend to obscure ambient noise. I applied the procedure of 'remove instrument response', which is grouping the zeros and poles of different instruments and remove them for further processing. Along with the instrumental response, I also applied the 'event' movement to obscure ambient noise. I processed seismograms on a daily basis at each station by applying the time domain normalization and band pass filter from 5 to 50 s.

Differing from Ambient Noise Tomography for Rayleigh wave that uses vertical component, Love wave has a horizontal particle motion (SH). Thus horizontal components are needed for extracting Love wave waveforms from ambient noise data. Seismograms on transverse component are needed for measuring the phase velocity of Love wave (**Figure 12**).

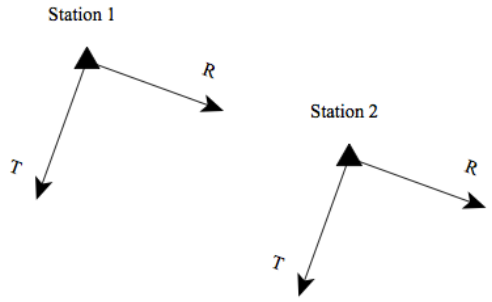

Figure 12. *Illustration of how transvers and radial components are defined between two stations*

Aldridge and Abbott (2009) described the basic theory of components rotation. A straight line can be defined by two stations (**figure 13**), which we can treat the line like a "ray path". The difference directions between north components and R or T component can be expressed by an angle φ (clockwise from north to the straight line).

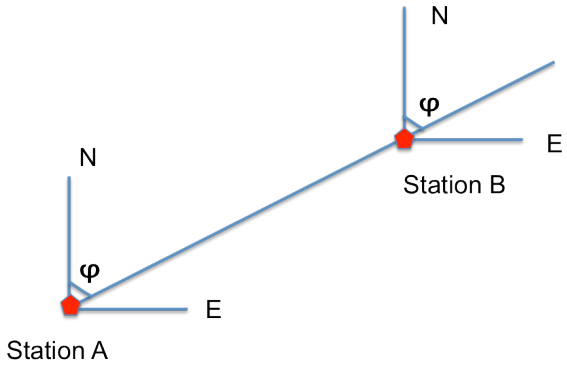

Figure 13. *Two stations define a straight line,* φ *is the angle from north components clock wise to the "ray path".*

According to this, we can calculate the components of rotation by the follow equations:

$$R = N\cos\varphi + E\sin\varphi$$
$$T = -E\cos\varphi + N\sin\varphi$$

R is the radial component of a station, T is transvers component, E and N are the east and north components from a same station. In my research, the Line that I applied to determine the angle φ is the great circle path between a station pair.

For Love wave, I only take the transverse component into processing (**Figure 14**). Compared to the raw data of the two stations in the figure, the transverse

component of KAZ (in the direction to WQIA) seemed much “nosier”, because the signal of interest is the random noise, so we applied a procedure of “event removal” for the transverse component.

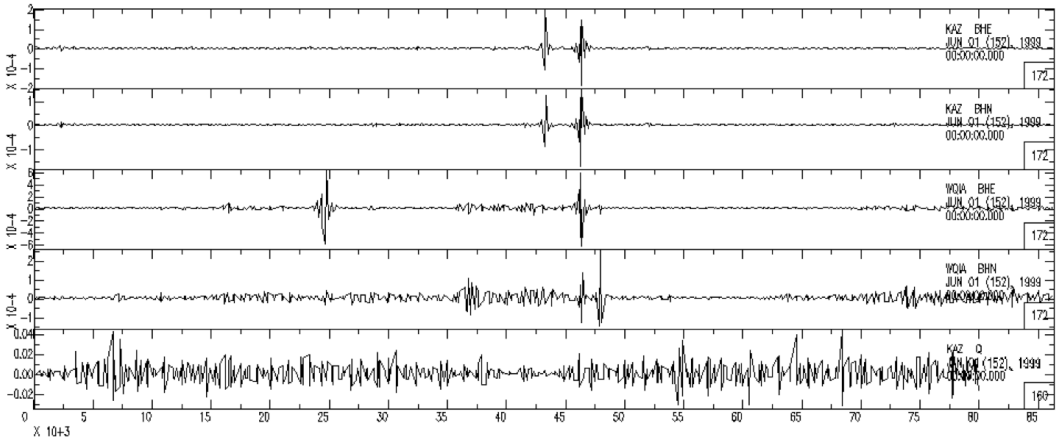

Figure 14. *An example of RT rotation for the station pair KAZ and WQIA. Figure (a) and (b) are the E and N components of KAZ. f (c) and (d) are the E and N components of WQIA. And figure (e) is the transvers component of this station KAZ. (The E and N components in the two stations are in raw data with earthquake events, and the rotated (T) component has been processed with event removal).*

After I finished the components rotation processing, the seismograms are transferred into frequency domain. The ambient noise is generally peaked near the primary (15s) and secondary (7.5) microseismic frequencies and rises at the period as long as 50 seconds (Figure 15) (Bensen, 2007). Then I applied the whitening

processing to the data that will broad the period band, which is mostly below 20-s for ambient noise for dispersion measurement (Lin, 2008).

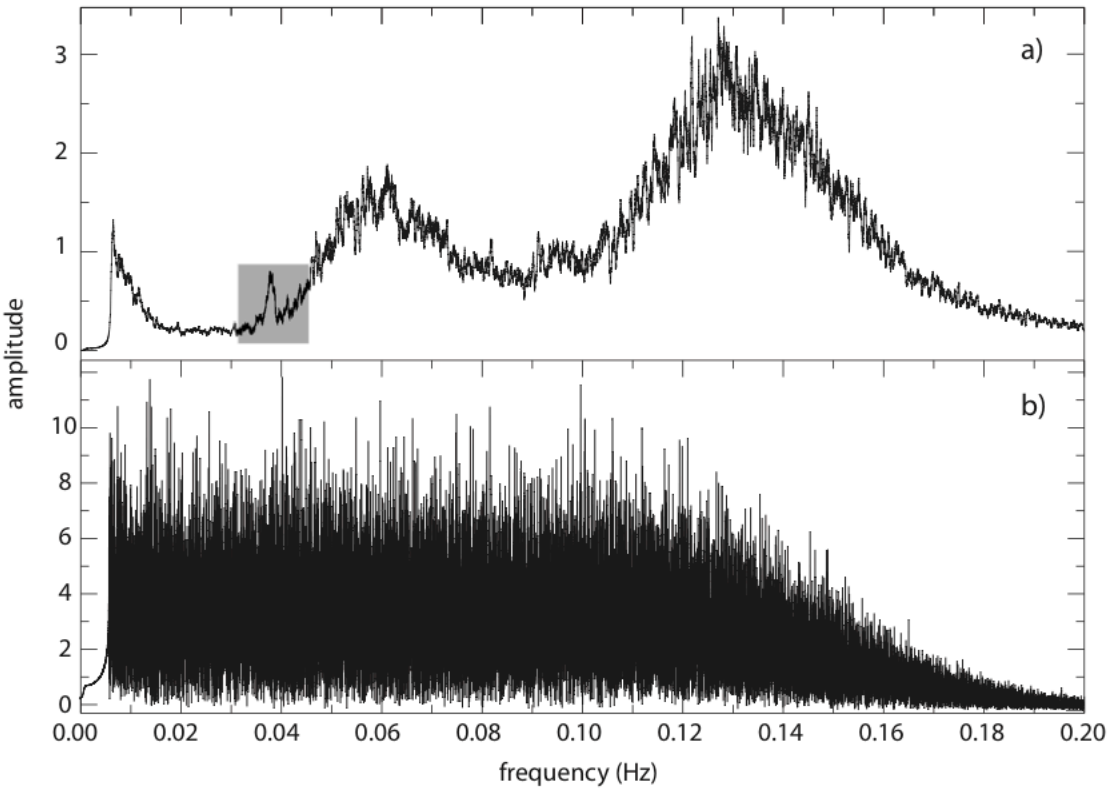

Figure 15*. a and b are the raw data and the spectrally whitened amplitude spectra (one sample per second). (Bensen, 2007)*

3.2.2 Cross-correlation and stacking

After finishing single station data processing, I cross-correlated transverse components of ambient seismic noise in frequency domain on a daily basis. Then the result of cross-correlation of same station pairs were inverted to time domain and added to each other. According to Bensen et al. (2007), stacking of 1-year data can produce reliable Green's

functions. Consequently, data are stacked every month and then every year. The total number of station pair is n(n-1)/2 with n as the number of stations which is 378 for this study. Due to different operation duration of those stations, there are comparatively less number of stations during the periods of the last three months of 1998 and the first five months of 2000. In most cross-correlations, Love waves appear symmetric on both positive and negative sides of the correlated waveforms (**Figure 16 and 17**). In the practical application of cross correlation, the results of daily cross correlation are stacked by month after cross correlation. After finishing the procedure of cross correlation, the data are stacked in order to enhance the 'event' of the Love wave and have a higher SNR. In my research, I stacked all the same station pairs by years (1998-2000), achieving a higher signal-noise ratio (**Figure 18**). In the figure 18, the waveform is symmetric in time, however, the amplitude is not perfectly same on both side of leg time, and this may be related to uneven distribution of seismic noise.

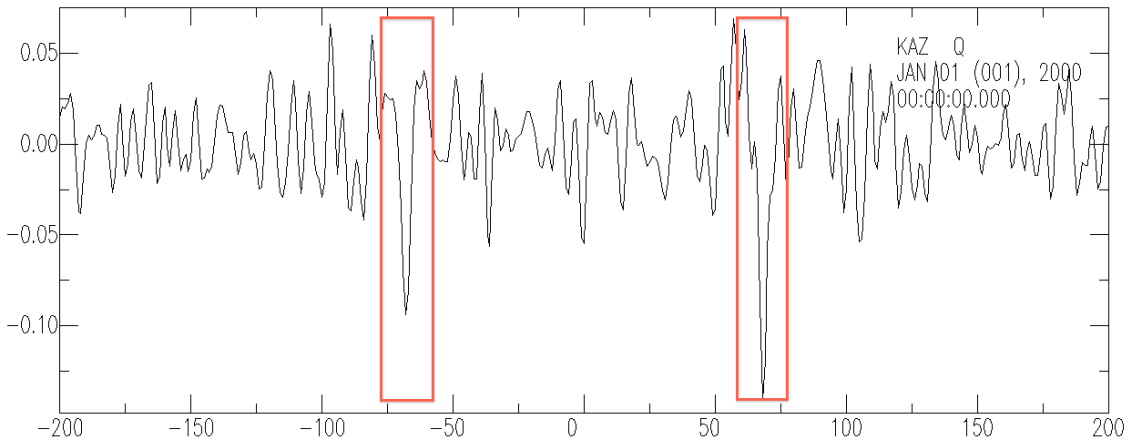

Figure 16. *An example of symmetric waveform after cross correlation and stack by month (station pair KAZ-WQIA).*

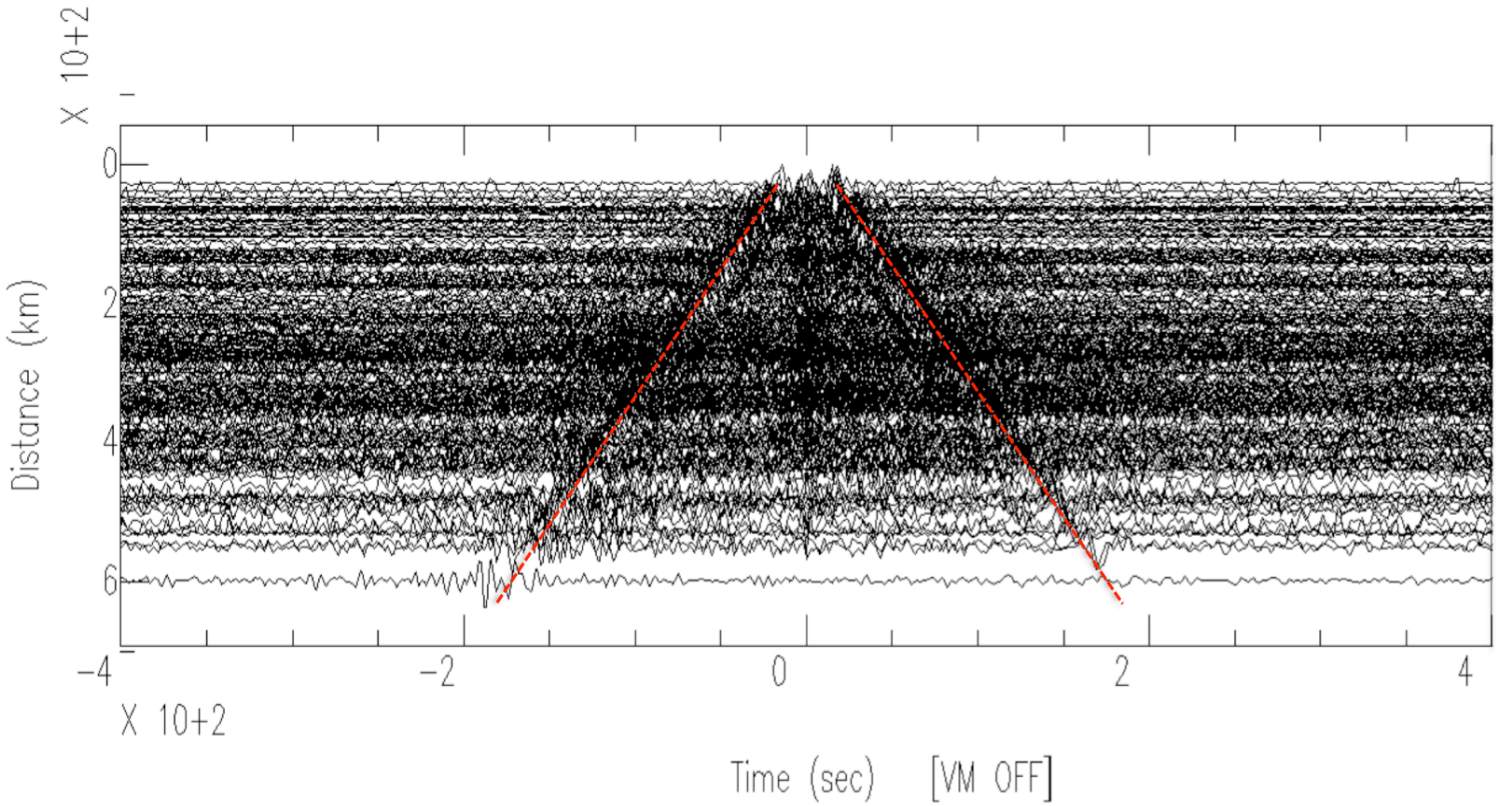

Figure 17. *Traces sort by distance for T-component.*

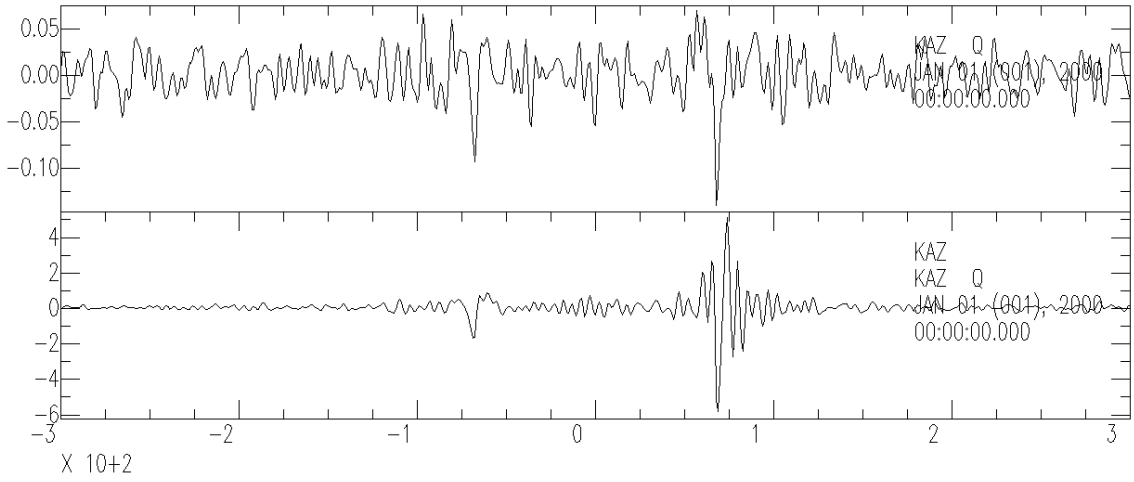

Figure 18. *Stacked cross correlations at station pair KAZ_WQIA. The upper figure is stacked by one month and the bottom one is stacked by one year.*

The lag time of Love wave signals is generally symmetric on both sides while the amplitude of the signals is often asymmetric. To improve the overall signal to noise ratio of Love waves, I windowed the stack at the range of -5000 to 5000 seconds, then folded the positive and negative part to form a single trace (**Figure 19**), which is used in obtaining phase velocity for each station pair.

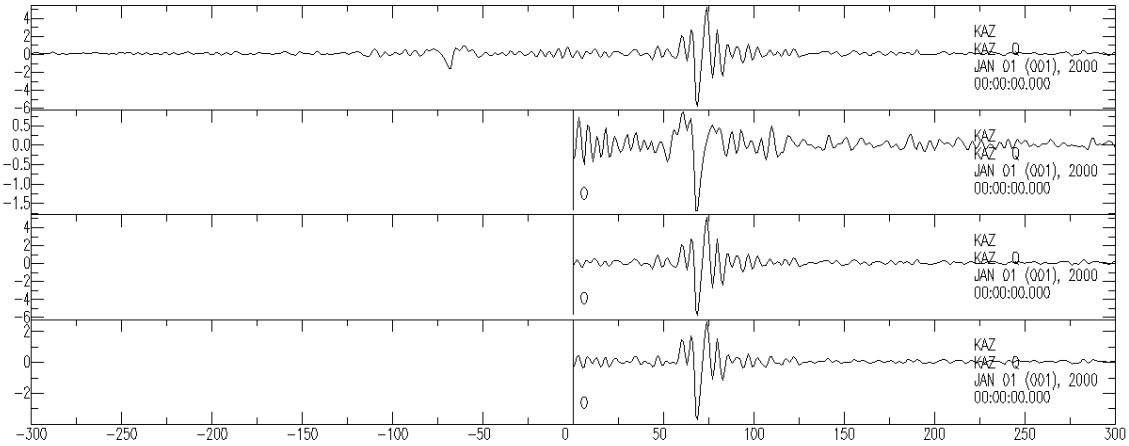

Figure 19. *An example of enhanced amplitude by stacking the positive and negative sides of the stacked cross correlations.*

4. Phase Velocity Measurements

4.1 Method

The phase velocity measurement is based on the theory of Green's Function. The theoretical relationship between cross correlation and estimated Green Functions has been expressed by Lin et al. (2008) as:

$$\frac{dC_{AB}(t)}{dt} = -G_{AB}(t) + G_{BA}(-t)$$
$$0 \le t < \infty$$

where C(t) is the ambient noise cross correlation and G(t) is the estimated Green's function. A and B are the stations pair, and the cross correlation results are symmetrical in waveform, which means the G (t) is an even function, so we have:

$$G_{AB}(t) = -\frac{dC_{AB}(t)}{dt}$$
$$G_{BA}(t) = -\frac{dC_{AB}(-t)}{dt}$$
$$0 \le t < \infty$$

The Green function can be derived as below and can be used for phase velocity measurement used.

$$G_{AB}(t) = -\frac{d}{dt}\left[\frac{C_{AB}(t) + C_{BA}(-t)}{2}\right]$$
$$0 \le t < \infty$$

Bensen et al. (2007) provided a method to measure the phase velocity based on the envelope function and measured group velocity. The function of phase velocity measurement contains a propagation term, an initial source phase and a phase ambiguity term. At instantaneous frequency ω, the equation can be expressed (Bensen et al., 2007):

$$\phi(t,\omega) = k\Delta - \omega t - \phi_s - \phi_a$$

where t is the travel time, Δ is the distance, k is the wavenumber, ϕ_s is the source phase and ϕ_a is the ambiguity term of phase. Let the wavenumber $k = \omega s_c$ and the group arrival time is $t_u = \Delta / U$, than the phase slowness is:

$$s_c = s_u + (\omega\Delta)^{-1}\left[\phi(t_u) + \phi_s + \phi_a\right]$$

where the group slowness s_u is known, and source phase ϕ_s is zero using ambient noise cross correlation. As for the ambiguity term ϕ_a , it should be a variable only depended on the times of π . It can be expressed as $n\pi$, and n can be decided based regional velocity model or phase velocity at very long period in the area. . Then phase velocity can be calculated using:

$$s_c = s_u + (\omega\Delta)^{-1}\left[\phi(t_u) + n\pi\right]$$

4.2 Phase velocity at station pairs

After processing the 24 months of ambient seismic noise data and stacking all cross correlations at each station pair, average phase velocity along a ray path between any two stations can be measured. I measured phase velocities for all station pairs at the periods of 8s, 10s, 12s, 14s, 16s, 18s, 20s, 25s, 30s and 35s. Figure 20 shows the ray paths between two station pairs, ESK2- TLG along the northern Tien Shan boundary to the Kazakh shield and DGE-KOPG in the southwest of the central Tien Shan range. Previous study (e.g. Vinnik et al., 2002, 2006; and Lisi and Li, 2012) shows that the region around ESK2-TLG has a generally higher velocity than the zone near the line of DGE-KOPG.

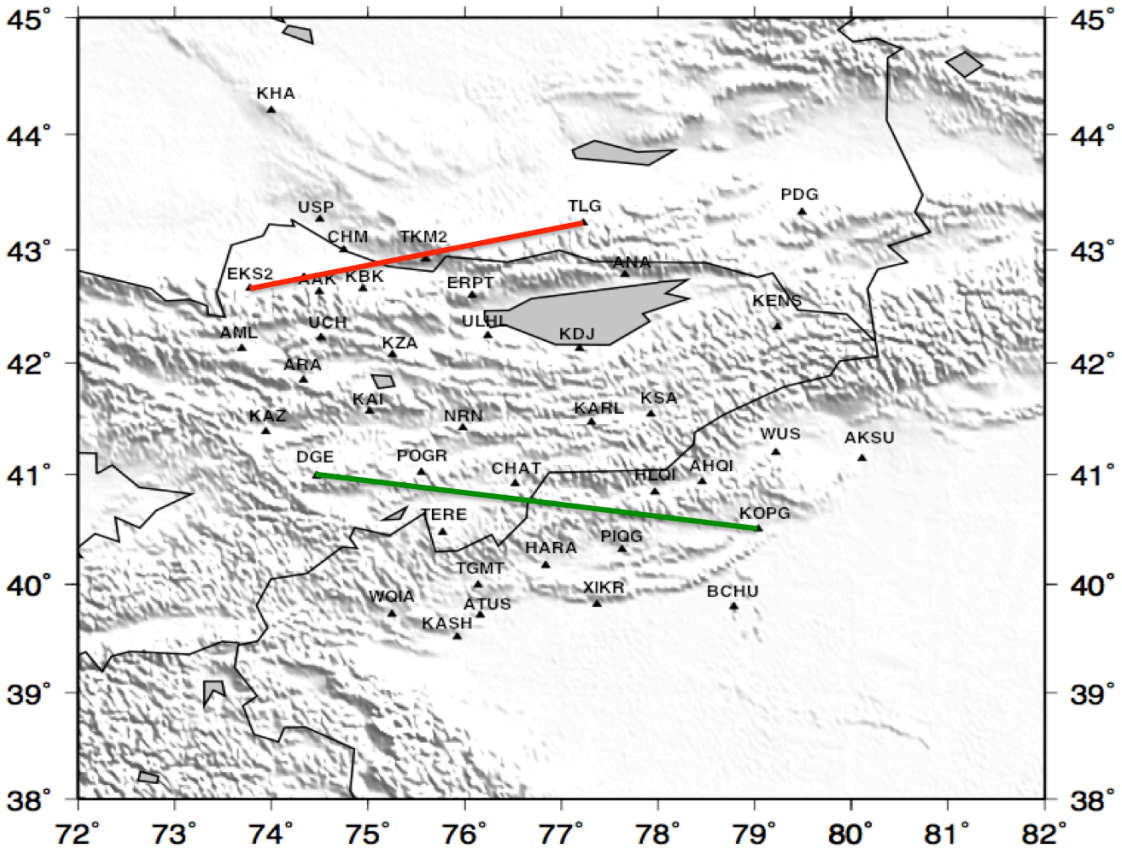

Figure 20. *Ray paths of two station pairs. The red line is for the station pair of ESK2-TLG and the green line is for DGE-KOPG.*

In order to compare the variation of phase velocity with the location and periods, I plotted phase velocities for both station pairs in Figure 21. It can be seen that phase velocity increases with period in a general sense, which makes sense because Love waves at longer periods sample the earth at greater depth and velocity generally increases with depth in the earth. At short periods (8-20s), the velocity has slight

differences. For longer periods (20-35s), the line of EKS2-TLG has a higher velocity. This is because the path of EKS2-TLG goes through a zone that has high velocity (Kazakh Shield).

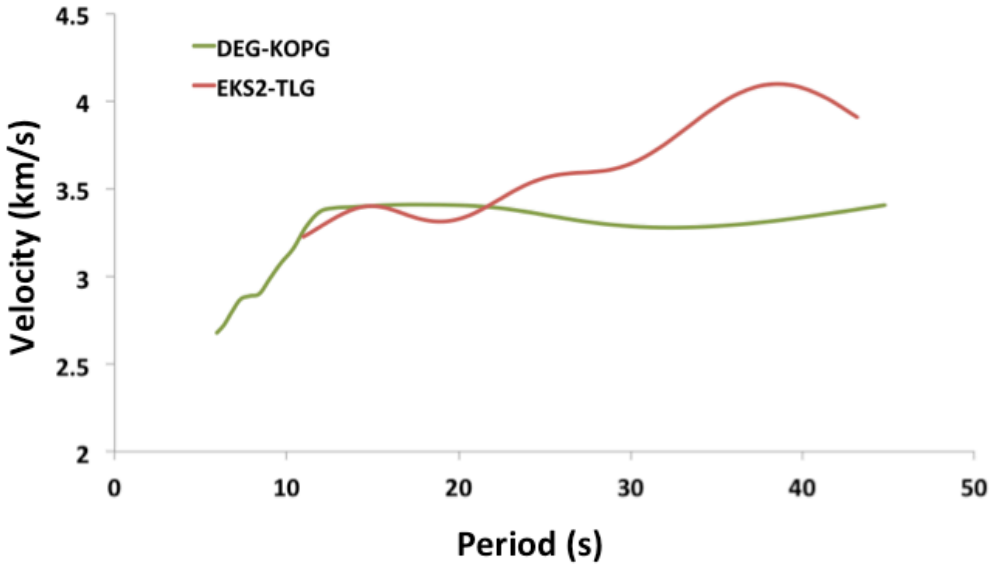

Figure 21. *Love wave phase Velocities of TWO different ray paths that shown in figure 20. Red line is for EKS2-TGL, and green line is for DGP-KOPG.*

Figure 22 shows average phase velocities from all the station pairs and the average velocities increase with period. The ambient noise data provide a period range from 6 to 35s at most station pairs and the corresponding average phase velocity changes from 3.2 km/s to 4 km/s (**Figure 22**).

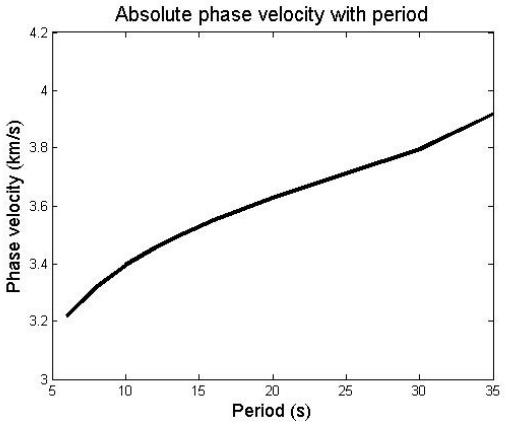

Figure 22. *Average phase velocity calculated from Ambient Seismic Noise from 6s to 35s.*

4.3 Phase velocity maps

After finding phase velocities for the periods from 8s to 35s at station pairs, I applied ambient noise tomography to the central Tien Shan using the method of Barmin et al. (2001).

The data used for the tomography is the stacked data (from September 1998 to July 2000) with the signal noise ratio higher than 20. Another criterion applied in selecting the data is the 3-wavelength limit, meaning the distance between a station pair should be greater than three times of the corresponding wavelength of the data. The available ray paths for tomography therefore vary with period (**Figure 23**). Ray paths at the mid-periods (16s-25s) have higher density within the station network and higher model resolution is therefore expected. As for shorter (8s-14s)

and longer (30s-35s) periods, the density of ray paths drops especially in the eastern and southern part of the study area. The distribution of ray paths helps to evaluate the robustness of measured phase velocities.

Lateral variation of phase velocities in the central Tien Shan is shown in Figure 24. The maps are velocity perturbations, which are relative to the average phase velocity at each period (**Figure 22**). The velocities features vary with period because different periods are sensitive to different depth of the earth. For shorter periods (8s to 12s), the velocities are more sensitive to the upper crust shear wave velocity. For longer periods, the velocity features are more sensitive to the deeper layers, for example, the lower crust.

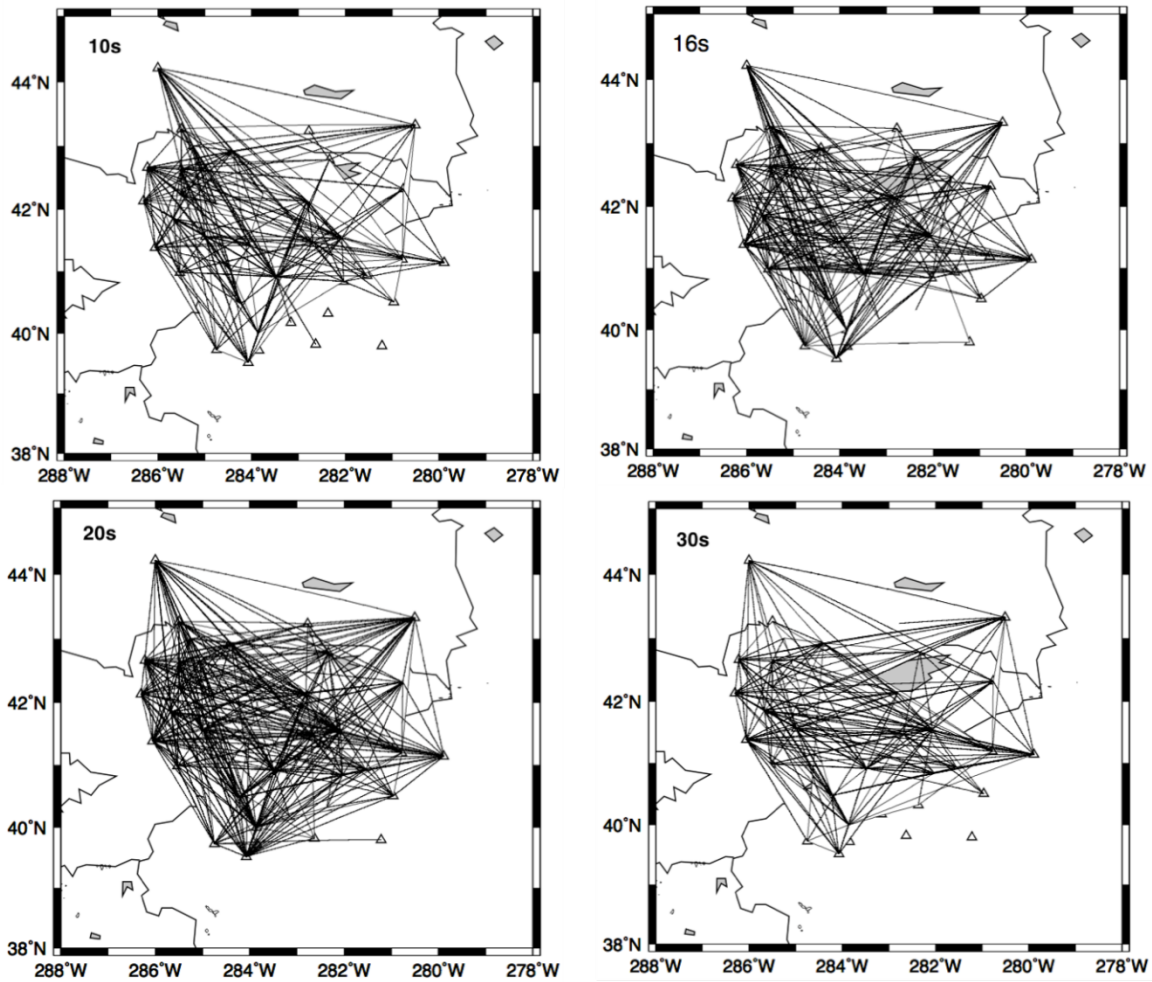

Figure 23. *Ray paths at periods of 10s, 16s, 20s, and 30s.*

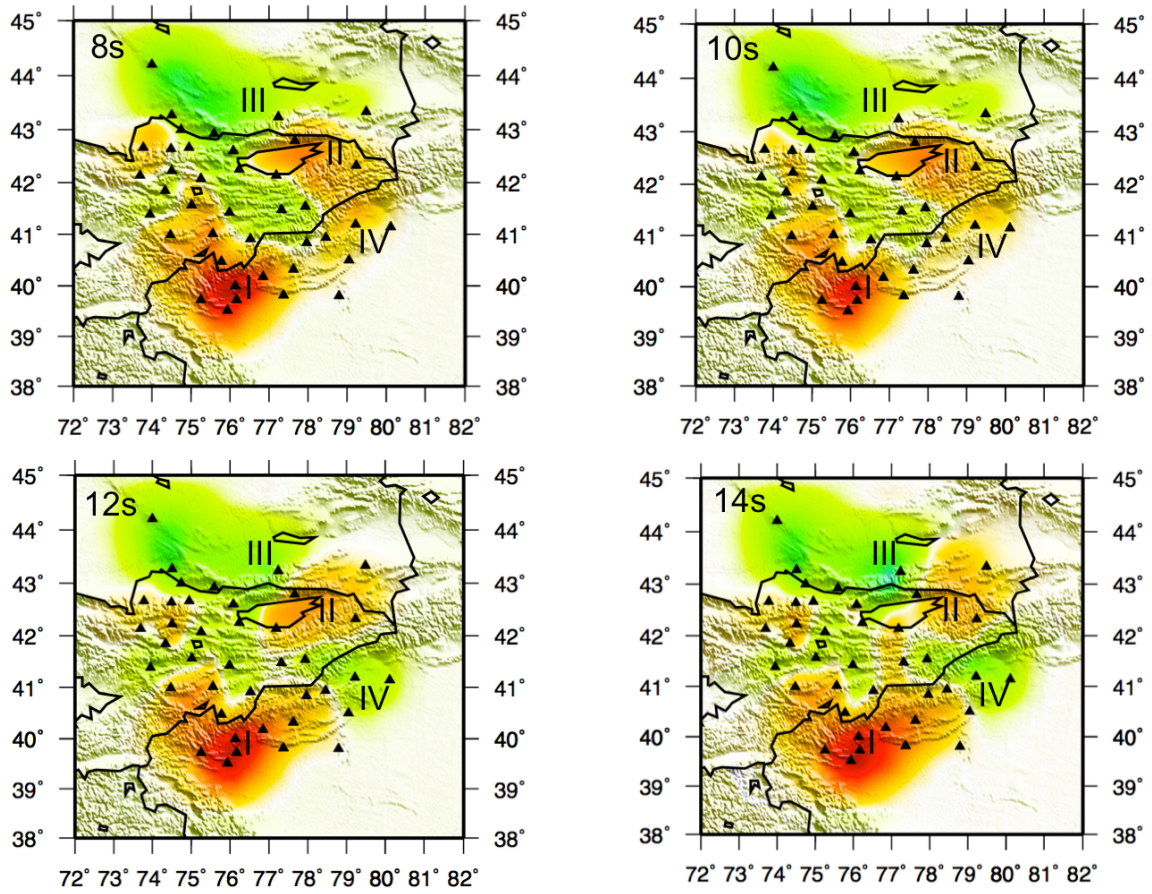

Figure 24. *Love wave phase velocity anomaly maps of the Tien Shan at periods from 8s to 35s.*

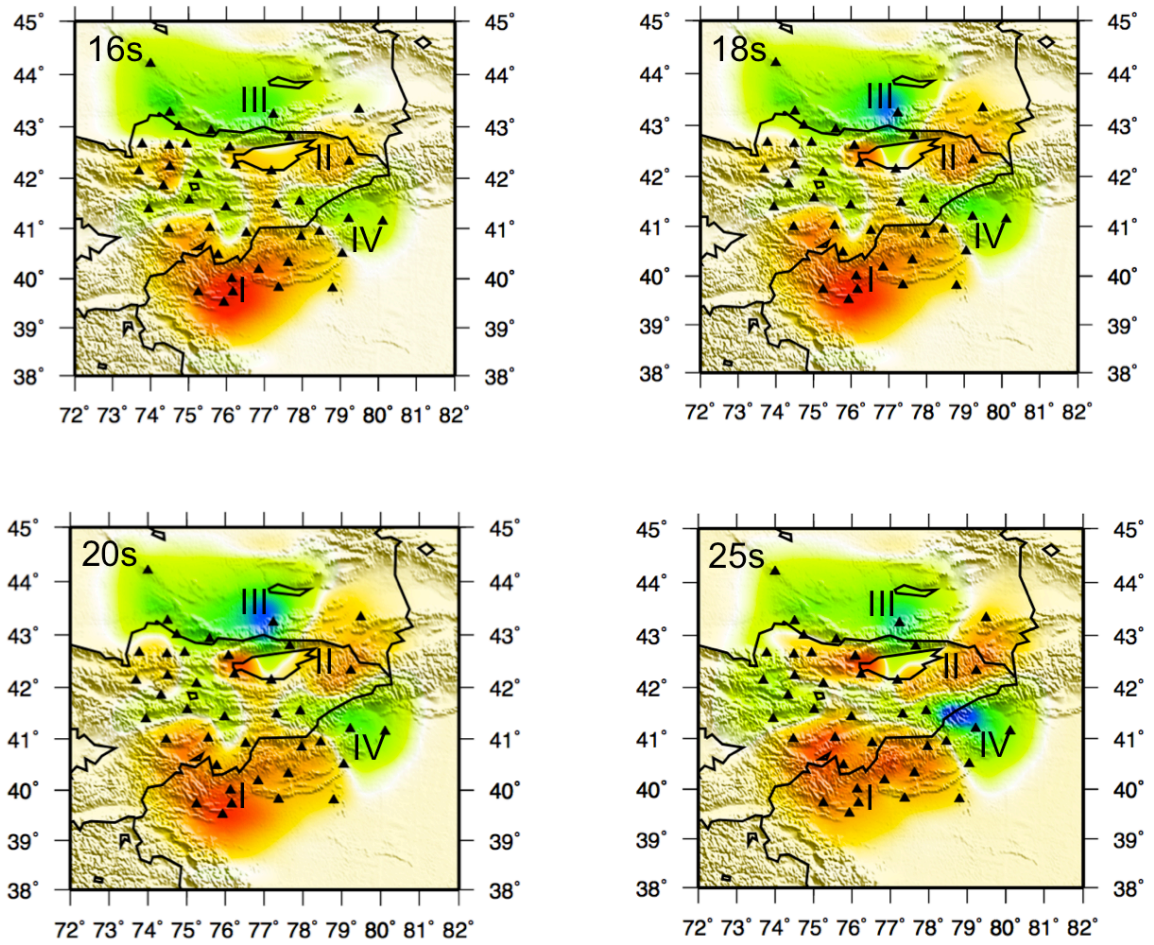

Figure 24. *Love wave phase velocity anomaly maps of the Tien Shan at periods from 8s to 35s. (Continued)*

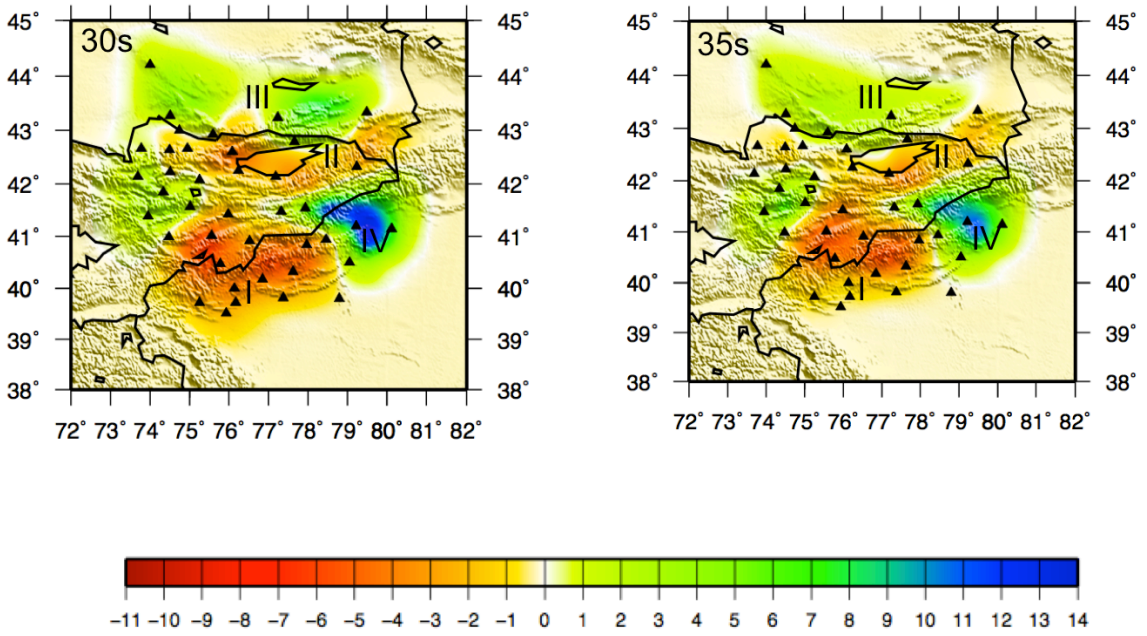

Figure 24. *Love wave phase velocity anomaly maps of the Tien Shan at periods from 8s to 35s. (Continued), the color scale is the velocity perturbation in %.*

On the maps of 8 to 20s periods, the results reveal a very low velocity zone to the southwest of the Tien Shan and along the northern boundary of the Tarim basin (**Zone I, Figure 24**). The low velocity anomaly in the southwest shifts northward beneath the high range of Tien Shan at long periods beyond 25s. Another consistently low velocity zone is imaged in the eastern Central Tien Shan range to the south of the Issyk Kul (**Zone II, Figure24**). Two pronounced fast anomaly areas are observed consistently at broad frequencies. The one in the Kazakh shield to the north of the Tien Shan (**Zone III, Figure24**) is imaged continuously from 8 to 35 s. The other fast anomaly to the southeast in the Tarim Basin (**Zone IV, Figure24**) is

imaged at periods above 12s and the anomaly becomes stronger at long periods (25-35 s).

5. Discussion

Lateral variations of Love wave phase velocity in the central Tien Shan reflect variable shear wave velocity across the area. The sensitivity of Love wave with depth is dependent on period (**Figure 25**). Love wave has a higher sensitivity at shallow depths than Rayleigh wave of the same period. Unlike Rayleigh wave sensitivity, which usually has sensitivity peaks at 1/3 of the given wavelength, Love wave sensitivity generally decreases with depth. Comparing the Love wave sensitivity curves at the three periods of 8s, 20s, and 30s in Figure 25, Love wave at 8s has the highest sensitivity above the depth of 15km; the sensitivity of 20s becomes the highest between 15km and 28km; Love wave at 30 s has the highest sensitive to the deeper part up to 50 km.

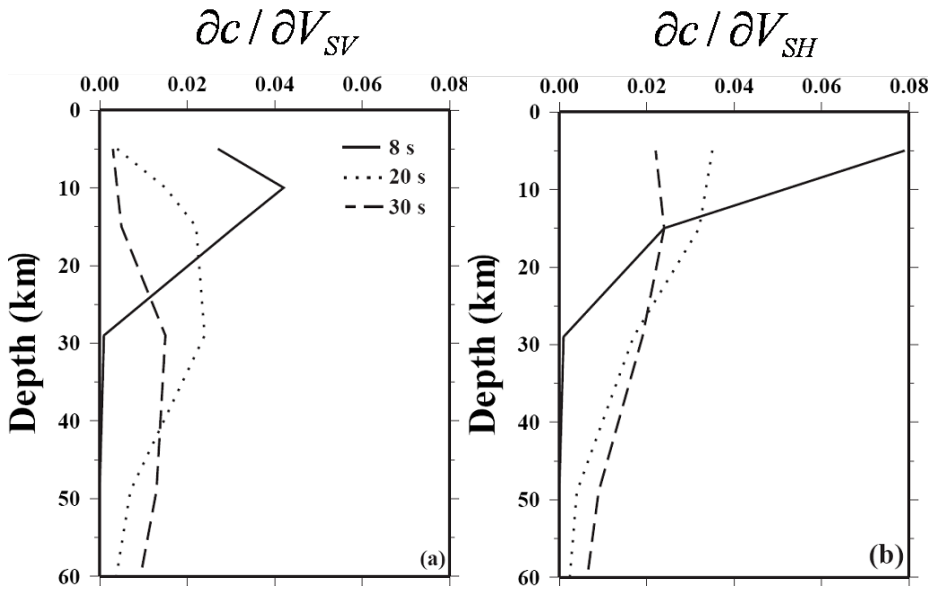

Figure 25. *Rayleigh wave (a) and Love wave (b) sensitivity kernels at 8, 20, and 30 s.*

According to the sensitivity depths of Love waves, the results of the ambient noise data from 8 to 35 s in the central Tien Shan can have sensitivity until the depth of 45-50 km. The crustal thickness in the central Tien Shan (Vinnik et al., 2006) (**Figure 3 d**) varies from 40 to 70 km. Thus, phase velocity anomalies from 8 to 35 s can reflect structure variation from upper to lower crust.

The high velocity zone that lies to the north of the Tien Shan is largely within the Kazakh Shield (**Zone III, Figure 24**). This high velocity anomaly is consistently imaged at all periods with increasing strength as small patches in the eastern part at intermediate periods. Such strength variation could be due to resolution change because ray paths in the east are less dense at shorter and longer periods, meaning the velocity anomaly in these periods might be underestimated. The property of the

crust of Kazakh Shield determines the high phase velocity zone. The crust beneath the Kazakh Shield is cratonic, which is more stable than the crust of the Tien Shan that is made of island arcs.

Another high velocity region is in southeast of the study area near the boundary of the Tien Shan with Tarim basin (**Zone IV, Figure 24**). This anomaly is continuously present from 12 s to 35 s with increasing strength at long periods. The relative low phase velocity in this area at 8 and 10 s is not significant, which could be smearing from the slow anomaly at the nearby Tien Shan range or could be caused by sediments at shallow depths. Similar to the fast anomaly in the Kazakh shield, this anomaly largely reflects the rigid cratonic crust beneath the Tarim. The anomaly moves slightly northward under the Tien Shan range at long periods, which might indicate the underthrusting of the Tarim lithosphere under the Tien Shan.

There is a strong low velocity zone (-3% to -6%) in the southwest of Tien Shan with the lowest values in the northern Tarim basin (**Zone I, Figure 24**). This low velocity zone is similar to that found in previous studies (Lei 2011; Lisi and Li 2012), but defers from the velocity measurements of Vinnik et al. (2004). This low velocity zone at short periods (8-20s) probably reflects thick sediment rocks in the northern Tarim. At long periods, the slow velocity zone moves northward to the Tien Shan range, indicating a slow mid-lower crust beneath the Tien Shan range or a thick crust beneath the range. In fact, Vinnik et al. (2007) found the thickest crust beneath

southwest of the central Tien Shan, consistent with the location of this slow anomaly. Since the Tien Shan was accreted from several arc blocks during Paleozoic, high water or volatile content is possible in the Tien Shan crust, which makes it slow and mechanically weak and easy to deform. In addition, the nearby Talas-Ferghana fault also indicates a weak crust around this area. The weak crust in southwest Tien Shan explains why GPS velocity in this area is faster than the north boundary of Tien Shan to Kazakh Shield because the crust here deforms easily and largely absorbs the compressional stress from the south caused by the collision between India and Eurasia plate.

The low velocity zone that is located in the central Tien Shan (**Zone I, Figure 24**) varies in shape and strength with period. At short periods (8-16s), the zone roughly focuses on the lake, caused by sediment in the Issky Kul. The slow anomaly extends to east and south mountain range with increasing period. The velocity perturbation decreases with period and the low velocity anomaly can still be seen at the 35s period (about 40km in depth). However, this result is significantly different from the model by Lei (2011), which shows a high P and S wave velocity around this area in the crust. Lei also suggested an up-welling of upper mantle beneath this area by the observation of a low velocity and high Poisson's ratio. The interpretation for this anomaly at longer periods is same as that in the southwest of the Tien Shan, reflecting a thick and slow mid-lower crust. However, my results have no resolution beneath the crust and cannot provide evidence for or against the hypothesis of the mantle plume beneath the central Tien Shan. The GPS velocity is also higher than the

north boundary (Zubovich et al., 2010) (**Figure 26, Zone A**) of Tien Shan to Kazakh Shield. The low velocities at the Tien Shan range suggest that the crust beneath the central Tien Shan is generally weaker than the surrounding area and thus can be deformed easily to build the current Tien Shan.

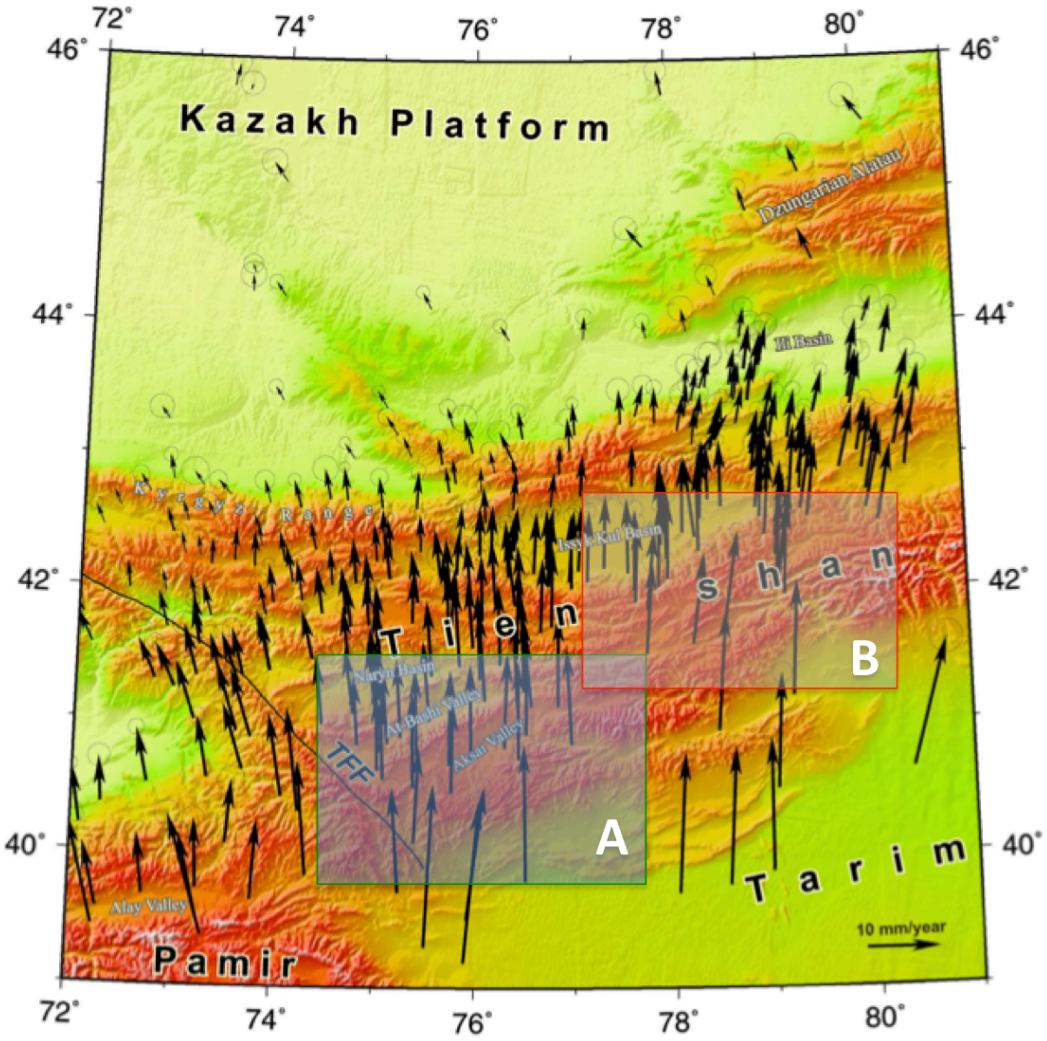

Figure 26. *Map of Tien Shan with GPS velocities relative to Eurasia. The Arrows show the direction and the length of the black bar indicates the velocity rate. Zone A and Zone B are the velocity zones within the Tien Shan area (Zubovich et al., 2010).*

The observation of a slow anomaly beneath the Tien Shan range and fast anomaly to the north and south of the central Tien Shan suggests that the weak Tien Shan crust is sandwiched between two rigid platforms, the Kazakh Shield and Tarim Basin. Previous GPS velocities in the central Tien Shan found that the gradient of velocity variations is steeper in southern part of the Tien Shan (**Figure 26, Zone B**)(Zubovich et al. 2010), indicating northward compression in this area. The northward push from the Tarim block compressed the weak Tien Shan against the strong Kazakh Shield) and caused significant shortening and deformation in the Tien Shan lithosphere to form the high intraplate mountain belt. Figure 26 is a cartoon for this mechanism. My study provide a weak indication for the possibility of a northward underthrusting of Tarim Basin but has no evidence for or against the hypothesis that mantle upwelling is the cause for the uplift of Tien Shan (**Figure 27**).

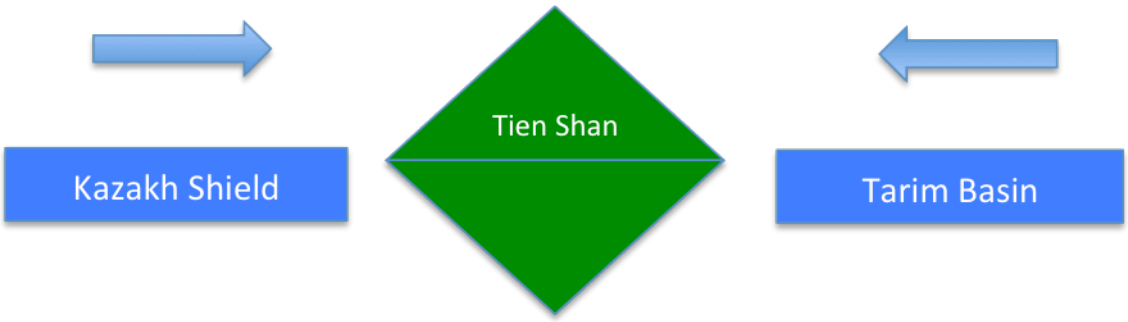

Figure 27. *Cartoon showing a weak Tien Shan is sandwiched between the strong Tarim basin and Kazakh shield with the NS compression.*

6. Conclusion

Ambient Seismic Noise Tomography for love wave phase velocity in the Tien Shan has identified four anomaly zones at periods of 8 to 35 s. Two high velocity anomaly zones locate near the south (Tien Shan to Tarim Basin) and north (Tien Shan to Kazakh Shield) boundaries of the Tien Shan, indicating fast and strong cratonic crust beneath the Tarim basin and the Kazakh shield. The study also observed two velocity zones, one is around the Issyk Kul Lake, and the other locates at the southwest Tien Shan bordered the northern Tarim basin. The slow anomalies at short periods (< 20 s) correlate with thick sediments in the northern Tarim and the lake. At longer periods, the slow zones indicate thick and weak crust beneath the Tien Shan range, implying the Tien Shan crust can be easily deformed.

These observations suggest that a thick and weak crust of the Tien Shan is sandwiched by two relatively rigid blocks, the Tarim and Kazakh crust. This is cohering to the suggestion of the Tien Shan mountain building is due to the shortening in the Tien Shan lithosphere caused by the NS compression. In addition, the study observes weak evidence for the underthrusting of the strong Tarim block on the south boundary of the Tien Shan. Due to the limitation of resolution in deeper layers, this study cannot test the hypothesis of mantle up-welling as the cause of the mountain building mechanism.

Reference:

Abdrakhmatov, K. Y., Aldazhanov, S. A., Hager, B. H., Hamburger, M. W., Herring, T. A., Kalabaev, K. B.,Makarov, V. I., Molnar, P., Panasyuk, S. V., Prilepin, M. T., Reilinger, R. E., Sadybakasov, I. S., Souter, B. J., Trapeznikov, Y. A., Tsurkov, V. Y., Zubovich, & A. V., 1996, Relatively recent construction of the Tien Shan inferred from GPS measurements of present-day crustal deformation rates, *Nature*, **384**, 450-453.

Aldridge D. F. & Abbott, R. E., 2009. Investigating the point seismic array concept with seismic rotation measurements. *Sandia Report*, SAN 2009-0798.

Allen, M. B., Vincent, S. J., & Wheeler, P. J., 1999. Late Cenozoic tectonics of the Kelpintage thrust zone: interactions of the Tien Shan and Tarim Basin, northwest China. *Tectonics*. **18**, 639–654.

Barmin, M. P., Ritzwoller, M. H., & Levshin, A. L., 2001. A fast and reliable method for surface wave tomography. *Pure Appl. Geophys*., **158**, 8, 1351-1375.

Bensen, G. D., 2007. Broad-band ambient noise surface wave tomography: technique development and application across the United States. Doctoral Thesis of University of Colorado, Department of Geological Science.

Bensen, G. D., Ritzwoller, M. H., Barmin, M. P., Levshin, A. L., Lin, F., Moschetti, M. P., Shapiro, N. M., & Yang, Y., 2007. Processing seismic ambient noise data to obtain reliable broad-band surface wave dispersion measurements, *Geophys. J. Int.* (2007) **169**, 1239–1260.

Burbank, D. W., McLean, J. K., Bullen, M., Abdrakhmatov, K. Y., & Miller, M. M., 1999. Partitioning of intermontane basins by thrust-related folding, Tien Shan, Kyrgyzstan. *Basin Research.* **11**, 75–92.

Bullen, M. E., Burbank, D. W., & Garver, J. I., 2003. Building the Northern Tien Shan: Integrated thermal, structural, and topographic constraints. *The Journal of Geology*, **111**, No. 2

Burtman, V. S., 1975. Structural geology of Variscan Tien Shan, USSR. *American Journal of Science,* **275-A**, 157–186.

Burtman, V. S., 2010. Tien Shan, Pamir, and Tibet: History and geodynamics of Phanerozoic Oceanic Basins. *Geotectonic*, **44**, 388-404.

Cotton, F., Avouac, J. P., 1994. Crustal and upper mantle structure under the Tien Shan from surface-wave dispersion. Physics of Earth and Planetary Interiors. **84**, 95-109.

England, P. C., & Houseman, G., 1986. Finite strain calculation of continental deformation, 2, comparison with the India-Asia collision zone, *J. Geophys*. Res., **94**, 17561-17579.

Fleitout, L. & Froidevaux, C., 1982. Tectonics and topography for a lithosphere containing density heterogeneities, *Tectonics*, **1**,21-56.

Guo, Z., Gao, X., Wang, W., Duan, Z., & Shi, H., 2010. S-wave velocity of the crust around Tianshan Mountains inverted from seismic ambient noise tomography. *Geophysics.* **55**, 3590-3598.

Heather, N., Andrew, C., Brian, B., & Erica, G., 2012. Seismic interferometry and ambient noise tomography in the British Isles. *Proceedings of the Geologist' Association*. **123**, 74-86.

Jiang, L.J., Li, Y.H., & Wu, Q.J., 2010. Shear wave splitting of central Tien Shan and its implications, *Chin. J. Geophys*., **53**(6): 10, 1399-1408.

Korjenkov, A. M., Arrowsmith, J. R., Crosby, C., Mamyrov, E., Orlova, L. A., Povolotskaya, I. E., & Tabaldiev, K., 2006. Seismogenic deatruction of the Kamenka medieval fortress, northern Issyk-Kul region, Tien Shan (Kyrgyzstan). *J. Seismol.* **10**, 431-442

Leonov, M. G., Morozov, Y. A., & Nikitin, A. V., 2007. Tectonic Deformation of Granites in the Tien Shan and Transbaikal Regions. *Doklady Earth Science*, **417A**, No. 9, 1348-1354.

Lei, J.S., & Zhao, D.P., 2007, Teleseismic P-wave tomography and the upper mantle structure of the central Tien Shan orogenic belt, *Phys Earth Planet Inter*, **162**: 165-185.

Lei, J., 2011. Seismic tomographic imaging of the crust and upper mantle under the central and western Tien Shan orogenic belt. *J. Geophys. Res.* **116**, B09305.

Li, A., & Chen, C., 2006. Shear wave splitting beneath the central Tien Shan and tectonic implications, *Geophys. Res. Lett*, **33**, L22303, doi: 10.1029/2006GL027717.

Li, H., Bernardi, F., & Michelini, A., 2010. Love wave tomography in Italy from seismic ambient noise. *Earthq Sci* **23**, 487-495

Li, H., Su, W., Wang, C., Huang, Z., & Lv, Z. 2010a. Ambient noise love wave tomography in the eastern margin of the Tibetan plateau. *Tectonophysics*. **419**, 194-204.

Li, Y., Wu, Q., Jiang, L., & Zhang, R., 2010b. Complex seismic anisotropic structure beneath the central Tien Shan revealed by shear wave splitting analyses. *Geophys. J. Int*. **181**, 1678-1686

Li, Z.W., Roecker, S.W., Li, Z.H., Wei, B., Wang, H., Gennady, S., & Vitaly, B., 2009, Tomography image of the crust and upper mantle beneath the west Tien Shan from the MAMAS broadband deployment: Possible evidence for lithospheric delamination. *Tectonophysics*, **477**: 49-57.

Lin, F., Moschetti, M.P., & Ritzwoller, M.H., 2008. Surface wave tomography of the western United States from ambient seismic noise: Rayleigh and Love wave phase velocity maps. *Geophys. J. Int*. **173**, 281–298

Lisi, A., & Li, A., 2013. Phase velocity and azimuthal anisotropy variations beneath the central Tien Shan. *Geophys. J. Int*. (In press)

Makeyeva, L.I., Vinnik, L.P., & Roecker, S.W., 1992. Shear-wave splitting and small-scale convection in the continental upper mantle, *Nature* **358**, 144-147.

Molnar, P., & Tapponier, P., 1975. Cenozoic tectonics of Asia: effects of a continental collision. *Science* **189**, 419-426.

Oreshin, S., Vinnik, L., & Peregoudov D., 2002. Lithosphere and asthenosphere of the Tien Shan imaged by S receiver functions. *Geophysical Research Letters*, **29**, No. 8, 32-1-32-4

Omuralieva, A., Nakajima, J. & Hasegawa, A., 2009. Three-dimensional seismic velocity structure of the crust beneath the central Tien Shan, Kyrgyzstan: Implications for large- and small-scale mountain building, *Tectonophysics* **456**, 30-34.

Pei, S., Zhao, J., Sun, Y., Xu, Z., Wang, S., Liu, H., Rowe, C.A., Toksoz, M.N., & Gao, X., 2007. Upper mantle seismic velocities and anisotropy in China determined through Pn and Sn tomography. *J Geophys. Res*. **98**, 15779-15795.

Roecker, S.W., Sabitova, T.M., Vinnik, L.P. Burmakov, Y.A., Golvanov, M.I., Mamatkanova, R., & Munirova, L., 1993. Three-Dimensional elastic wave velocity structure of the western and central Tien Shan. *J. Geophys. Res*. **98**, 15,779-15,795.

Sabitova, T. M., Lesik, O. M., & Adamova, A. A., 1998. Veolocity and Density heterogeneities of the Tien-Shan Lithosphere. *Pure and Applied Geophysics*, **151**, 539-548

Shapiro, N. M., Campillo, M., Stehly, L., & Ritzwoller, M. H. 2005. High-resolution surface-wave tomography from ambient seismic noise. *Science*, **307**(5715), 1615–1618.

Sobel, E., & Dumitru, T. A., 1997. Thrusting and exhumation around the margins of the western Tarim basin during the India-Asia collision, *J. Geophys. Res.*, **102**, 5043-5063.

Tommasi, A., Tikoff, B., & Vauchez, A., 1999, Uper mantle tectonics: 3-D deformation, olivine crystallographyic fabrics and seismic properties. *Earth Planet. Sci. Lett*, **168**, 173-186

Tromp, J., Luo, Y., Hanasoge, S., & Pater, D., 2010. Noise cross-correlation sensitivity kernels. *Geophys. J. Int*. **183**, 791-819.

Vinnik, L., Reigber, C., Aleshin, I., Kosarev, G., Kaban, M., Oreshin, S., and Roecker, S., 2004. Receiver function tomography of the central Tien Shan, Earth Planet. Sci. Lett., **225**, 131–146.

Vinnik, L. P., Roecker, S., Kosarev, G. L., Oreshin, S. I., & Koulakov, I. Y., 2002. Crustal structure and dynamics of the Tien Shan. *Geophysical Research Letter*, **29**, No. 22, 4-1-4-4

Vinnik, L. P., Aleshin, I. M., Kaban, M. K., Kiselev, S. G., Kosarev, G. L., Oreshin, S. I., & Reigber, Ch., 2006. Crust and Mantle of the Tien Shan from Data of the Receiver Function Tomography, *Physics of the Solid Earth*, **42**, No. 8, 639-651.

Vinnik, L. P., Aleshin, I. M., Kiselev, S. G., Kosare, G. L., & Makeyeva, L. I., 2007. Depth localized azimuthal anisotropy from SKS and P receiver function: The Tien Shan. *Geophys. J. Int*. **169**, 1289-1299

Weaver, R. L., & Lobkis, O. I. 2001. Ultrasonics without a source: Thermal fluctuation correlations at MHz frequencies. *Phys. Rev. Lett*., **87**(13), 134301(4)

Xiao, W., Windley, B.F., Allen, M.B., & Han, C., 2012. Paleozoic multiple accretionary and collisional tectonics of the Chinese Tienshan orogenic collage, *Gondwana Res*(2012), doi:10.1016/j.gr.2012.01.012.

Xu, J.R., Zhao, Z.X, & Ishikawa, Y., 2008. Regional characteristics of crustal stress field and tectonic motions in and around Chinese mainland, *Chin. J. Geophys*., **51**, 770-781.

Xu, Y., Li, Z., & Roecker, S. W., 2007. Uppermost mantle structure and its relation with seismic activity in the central Tien Shan. *Geophysical Research Letter*. **34**, L1304.

Xu, Y., Liu, F., Liu, J., & Chen, H., 2002. Crust and upper mantle structure beneath western China from P wave travel time tomography. *J. Geophys. Res*. **97**, 19909-19928.

Yang, S.M., Li, J., & Wang, Q., 2008. The deformation pattern and fault rate in the Tienshan Mountains inferred from GPS observations, *Sci. China, D: Earth Sci*., **51**, 1064-1080.

Yang, Y., & Liu, M., 2002. Cenozoic deformation of the Tarim plate and the implications for mountain building in the Tibetan Plateau and the Tien Shan, *Tectonics*, **21**, No. 6, 1059.

Zubovich, A.V., Wang, X., Scherba, Y.G., Schelochkov, G.G., Reilinger, R., Reigber, C., Mosienko, O.I., Molnar, P., Michajljow, W., Makarov, V.I., Li, J., Kuzikov, S.I., Herring, T.A., Hamburger, M.W., Hager, B.H., Dang, Y., Bragin, V.D., & Beisenbaev, R.T., 2010. GPS velocity field for the Tien Shan and surrounding regions. *Tectonics*. **29**, TC6014, doi: 10.1029/2010TC002772.